Multi Phenomena Melt Pool Sensor Data Fusion for Enhanced Process Monitoring of Laser Powder Bed Fusion Additive Manufacturing

Aniruddha Gaikwad¹*, Richard J. Williams², Harry de Winton², Benjamin D. Bevans^{1,3}, Ziyad Smoqi¹, Prahalada Rao^{1,3}, Paul A. Hooper²

Abstract

Finding actionable trends in laser-based metal additive manufacturing process monitoring data is challenging owing to the diversity and complexity of the underlying physical interactions. A single monitoring solution that captures a particular process phenomenon, such as a photodiode that tracks melt pool intensity, is not alone capable of evaluating process stability or detecting flaw formation with sufficient precision for routine application in industry. In this work, to improve flaw detection performance, we adopted a data fusion approach that captures multiple process phenomena. To demonstrate this, we acquired data from laser powder bed fusion (LPBF) builds of cylindrical specimens produced with different laser spot sizes, emulating defocusing due to process faults such as thermal lensing. The resulting specimens had porosity of varying severity, quantified by postbuild non-destructive X-ray computed tomography, Archimedes density measurements, and destructive metallographic characterization. During the build, the melt pool state was monitored with two coaxial high-speed video cameras and a temperature field imaging system. Physically intuitive low-level melt pool signatures, such as melt pool temperature, shape and size, and spatter intensity were extracted from this high-dimensional, image-based sensor data. These process signatures were subsequently used as input features in relatively simple machine learning models, such as a support vector machine, which were trained to detect laser defocusing, and in addition, predict porosity type and severity. The results show that the data fusion approach significantly enhanced system performance by reducing the overall false positive rate from ~ 0.1 to ~ 0.001 without sacrificing the true positive rate (~ 0.90). These results were at par with a black-box, deep machine learning approach (convolutional neural network).

Keywords: Laser powder bed fusion, laser defocus, thermal lensing, porosity, high-speed melt pool imaging, spatter, melt pool temperature, sensor data fusion.

¹Mechanical and Materials Engineering, University of Nebraska-Lincoln, Lincoln, NE, USA.

²Mechanical Engineering, Imperial College, London, UK.

³Grado Department of Industrial and Systems Engineering, Virginia Tech, Blacksburg, VA, USA.

^{*} Corresponding author: mailto:aniruddha.gaikwad@huskers.unl.edu

1 Introduction

1.1 Motivation

Laser powder bed fusion (LPBF) is an additive manufacturing process in which metal powder is deposited (raked or rolled) on a substrate and selectively melted using a laser, layer-upon-layer, to create a three-dimensional object (Figure 1) [1]. Despite significant advantages over conventional subtractive and formative manufacturing, the use of LPBF parts in mission-critical applications, e.g., aerospace and energy generation industries, is currently limited by inherent process flaws, such as porosity and distortion in shape, among others [2].

In-process monitoring offers an avenue for rapid detection and characterization of flaw formation within LPBF parts, as well as facilitates assessment of the impact of flaws on part integrity [3-8]. However, finding robust and industrially useful trends within in-process monitoring data is challenging due to the complexity of the underlying physical interactions in LPBF [9].

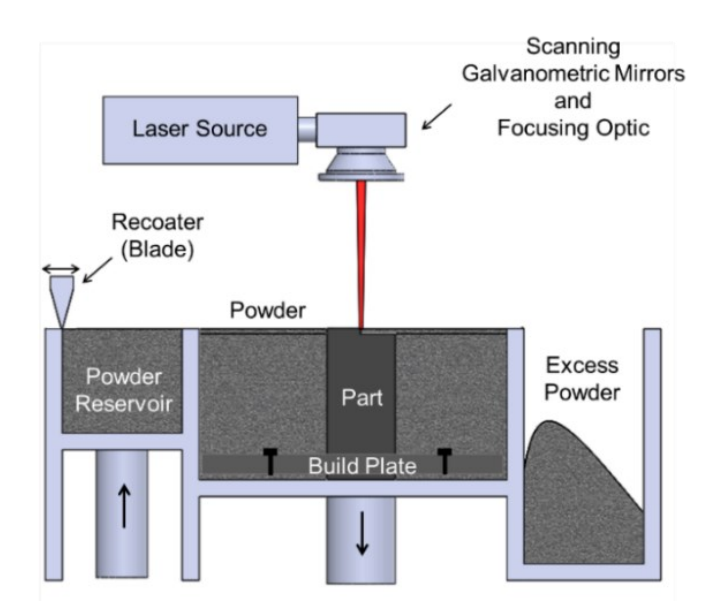


Figure 1: Schematic representation of the laser powder bed fusion (LPBF) process.

The aim of this work is to demonstrate that the flaw detection performance improves significantly on adopting a data fusion approach. We show that capturing sensor data representative of multiple process phenomena and combining the data signatures within relatively simple machine learning

methods reduces false positive rates to acceptable levels, thus enhancing performance of the flaw detection system, and enabling rapid, robust, and industrially relevant decision-making.

1.2 Background and Challenges

Flaw formation in LPBF occurs despite extensive process optimization, process standardization, and automation due to uncontrolled variation in the process [10]. These variations can be systematic or stochastic in nature [11]. Systematic variation can be further classified into two groups: (i) machine-related, and (ii) part geometry- or scan path-related. An example of a frequent machine-related systematic variation is when gaseous by-products (soot) released from powder fusion builds up on the laser optical window. The soot absorbs a portion of the laser energy which causes localized heating and thermal expansion of the optical window, changing the focal length of the optical system (known as thermal lensing) [12-14]. These anomalies in the laser focus often lead to poor material consolidation, which in turn results in lack-of-fusion porosity [14].

Part geometry and scan path variations lead to uncontrolled variation in part temperature during the process, potentially caused by short scan vectors or long interlayer times [11, 15]. These machine- and geometry-related variations cause the machine to operate at the edge of its processing parameter window, where a low part temperature results in lack-of-fusion porosity, or high part temperature increases the keyhole depth resulting in keyhole porosity [16-18].

An example of a stochastic flaw is when spatter particles ejected from the interaction of powder and laser settle elsewhere on the powder bed. These spatter particles can impede the laser in fusing material, and potentially lead to porosity [11, 19]. Additionally, systematic variation often interacts with stochastic variation, which increases the frequency and severity of stochastic flaw formation mechanisms; it is therefore difficult to treat each cause of variation in isolation.

In-process monitoring, and flaw detection is proposed as a potential method to ensure process stability, and isolate, characterize (identify) and measure flaw formation [3-8]. The advantage and need for in-process monitoring in LPBF is two-fold. First, if flaws can be detected as they form, they can potentially be corrected in real-time through a feedback control mechanism. Second, expensive post-process characterization, such as X-ray computed tomography and destructive metallography, for qualifying part quality can be minimized through substitution with in-process data [20, 21].

Currently, effective in-process monitoring in LPBF is hampered due to the complexity of the underlying physical interactions, and lack of scalability and transferability of the methods developed across various materials, machines, and geometries [22]. Indeed, most approaches in the literature focus on signatures from one sensing modality that captures a particular phenomenon [4]. For example, a photodiode to track melt pool intensity, or a pyrometer to capture melt pool temperature [8, 23, 24]. Hence, the existing sensing and monitoring approaches do not effectively capture the multi-phenomena nature of LPBF, which leads to degradation in predictive performance.

There are two main challenges with in-process monitoring in LPBF: (i) a large volume and variety of data is often acquired during processing – a Big Data problem, and (ii) difficulty in extracting relevant trends from the sensor data for practical decision-making [25]. In this context, a process monitoring system should successfully detect an anomaly (high true positive rate), whilst at the same time, not produce false alarms (high false positive rate) that lead to a part being scrapped unnecessarily. Moreover, the monitoring approach must not cause delays to the LPBF process, nor require long-term storage of excessive amounts of data, and should not take so long to analyze the data that the practical utility for decision-making diminishes.

Considering the Big Data challenge in LPBF, making a simple cuboid-shaped part measuring 2.5 cm × 2.5 cm × 2.5 cm typically requires melting over 5 km of 250,000 individual tracks at laser

scanning speeds close to 1 meter per second [10]. For this small part, a typical photodiode-based melt pool monitoring system would acquire raw data in the order of 1 GB, and a camera-based melt pool monitoring system would acquire >1 TB of data. A process anomaly at any point along that 5 km of scan tracks in the part could lead to a flaw that inhibits its functionality. Hence, the second challenge is in detecting and tracking robust and industrially relevant trends within in-process monitoring data.

Whilst machine learning has been used extensively for sensor-based monitoring and flaw detection research in LPBF [22, 26, 27], the primary difficulty in acting on in-process monitoring data lies in the difference between true positive and false positive rates [28]. The ideal monitoring system is not one that maximizes true positive rate of flaw detection at all costs, but one that minimizes the false positive rate, and additionally, maintains an acceptable true positive rate. Detection of actual flaws (true positives) must be sufficiently consistent to ensure significant defects are rarely missed. At the same time, false positives (detecting a flaw that is not physically present in the part) must be reduced to the point where parts are not rejected unnecessarily, making the system uneconomical. In practical LPBF manufacturing, the goal is to produce the best possible quality parts and in turn reduce flaw formation, such as porosity. Hence, for a given in-process detection system, this means that there are many more opportunities for making false positive errors than for making true positive detections.

1.3 Objective and Hypothesis

The objective of this work is to demonstrate that a significant improvement in flaw detection performance is achieved by adopting a data fusion approach which integrates the signatures acquired from high-speed imaging cameras and a melt pool temperature field imaging system. These sensors capture different phenomena occurring in the laser-material interaction zone, including melt pool temperature, the dynamical behavior of the melt pool, and spatter [29]. Through characterization of multiple phenomena, i.e., melt pool morphology (size, shape, and intensity), spatter characteristics (area, number, and intensity), and melt pool temperature distribution, these signatures can be subsequently used as inputs within simple machine learning approaches to predict deviations in the laser spot size and severity of porosity.

The ability to readily extract physically intuitive signatures from high-dimensional and high-volume imaging data and leveraging these signatures for process monitoring in relatively simple machine learning algorithms enables the rapid detection of process faults that can potentially cause flaw formation. Moreover, the coupling of physics-based data signatures with tractable models makes the approach interpretable, and potentially, transferable across different materials and LPBF machines. In other words, precise flaw prediction with both low false positive and high true positive rates is achieved by using physics-based features within simple machine learning models with low computational burden.

As part of this objective, we test two hypotheses: (1) the fusion of multi-phenomena data significantly improves detection of processing faults and reduces false positive rates to acceptable levels compared to using one type of data signature alone; (2) physically intuitive and low-level sensor signatures when used with simple and computationally light machine learning models, can

detect processing faults and flaws with an accuracy comparable to complex and computationally demanding approaches, such as deep learning-based convolutional neural networks.

To test these hypotheses and demonstrate the effectiveness of the approach we apply it to the detection of changes in the laser spot size, a common LPBF machine problem caused by thermal lensing [12-14]. We also use the presented approach to classify the porosity in terms of its type and severity. The results are compared with a complex black-box, deep learning-based machine learning model (convolutional neural network) that directly uses the raw melt pool images.

The paper is organized as follows. In Sec. 2, we describe the methods, encompassing the experiments conducted, post-processing of builds, in-process monitoring setup consisting of the high-speed melt pool imaging and melt pool temperature field imaging sensors, capturing physics-informed process signatures, and machine learning models used for process monitoring. Sec. 3 details the results demonstrating the effectiveness of the presented approach in detecting laser defocusing, and predicting level of porosity in specimens, as well as discussing the significance of these findings. Finally, conclusions are summarized in Sec. 4.

2 Methods

This section reports the experimental setup and design of experiments (Sec. 2.1), in-process sensor data analysis (Sec. 2.3), and post-process material characterization (Sec. 2.1.3). A detailed explanation of the machine learning approach used for detection is provided Sec. 2.4.

2.1 Experiment design

The experiments in this work were designed with the aim of emulating thermal lensing, a common type of process failure that causes a change in laser spot size at the build plane, reducing energy density, and in turn resulting in lack-of-fusion porosity formation [12-14].

2.1.1 Background – Deviation in laser spot size in LPBF

Flaw formation, including porosity in LPBF has its origin in complex phenomena, such as, balling, Marangoni convection, Plateau-Rayleigh effect, spatter, denudation etc. These phenomena are fundamentally driven by the laser-material interactions at the melt pool level [19]. In LPBF the diameter of the laser beam at the build plane is a critical factor that influences the behavior of the melt pool and ultimately the functional quality of a part [30].

Extensive theoretical and experimental results have shown that the temperature, shape, size, and spatter behavior of the melt pool have a consequential effect on solidification rates (microstructure evolution), surface integrity, thermomechanical effects (residual stresses and distortion) [19, 31-39]. Hence, maintaining an optimal laser beam diameter that remains stable throughout the build is critical for producing quality parts. As will become evident in Sec. 2.3, this work leverages characteristics of the melt pool and spatter behavior that are evocative of the fundamental physical phenomena that govern porosity formation.

To focus the laser beam on the powder bed, LPBF machines either use a f-theta lens or a dynamic-focusing stage. Both systems aim to maintain a constant laser beam diameter on the powder bed irrespective of the angle of incidence of the laser beam as it emerges from the galvanometric mirrors. The appropriate beam diameter (Φ_d) is obtained by adjusting the distance between the waist of the laser beam and top of the powder bed, termed the laser focus height (L_{fh}).

In an LPBF machine, the laser focus height is controlled via a focusing stage within in the laser optical train. Ideally, the laser beam is focused such that its waist converges on the powder bed, thus maximizing the energy delivered by the beam per unit area, called the areal energy density [J·mm⁻²] [40]. This allows the fastest processing speed whilst maintaining a small minimum feature size (part resolution).

The effect of laser focus height on part quality is shown in Figure 2. If the beam is focused above the powder bed, then the diameter of the laser beam (area) projected on the powder bed increases. Hence, for a fixed laser power, the energy delivered by the laser is spread over a larger area, which may lead to incomplete fusion of the powder material (Figure 2(a)) [41]. Insufficient fusion manifests in irregular-shaped pores of diameter ranging from 30 µm to 500 µm (and above for severe cases). Such pores shown in Figure 2(a) are called lack-of-fusion flaws [42]. A similar effect is seen if the focal plane of the laser is below the powder bed, except the laser beam is converging rather than diverging when it hits the surface.

Correct focusing combined with well optimized processing parameters (laser power, velocity, and hatch spacing) leads to very little porosity as seen in Figure 2(b). Excessive energy density from poorly optimized parameters will lead to keyhole melting, increasing the probability of the formation of small pinhole-shaped pores (Figure 2(c)) [43]. Exposure to excessive energy density is also linked to pinhole porosity due to escaping gas dissolved in the melt pool (gas porosity)[7].

There are two main reasons that the laser focus may depart from its setpoint, changing the laser diameter at the build plane. The first reason for the change in laser spot size during a build is an effect known as *thermal lensing* [12-14]. In LPBF machines, a continuous flow of inert gas, typically argon or nitrogen, is maintained over the powder bed to avoid oxidation of the material and aid removal of process byproducts such as soot and spatter.

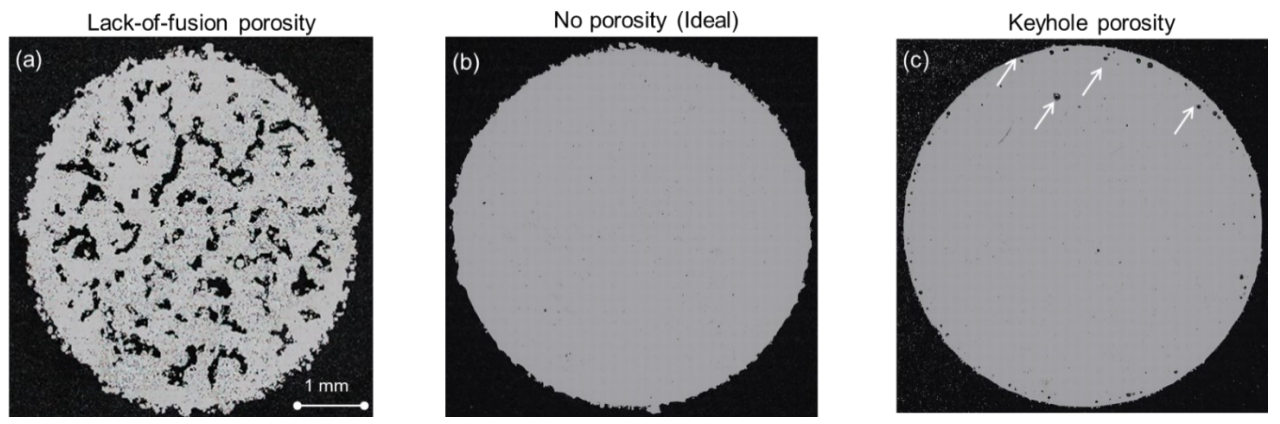


Figure 2: Optical micrographs showing different porosity regimes generated through alteration of the laser focus height.

It is difficult to remove all these byproducts. As a result, soot tends to accumulate on the colder regions of the machine, such as the optical window. The soot accumulated on the optical window will absorb a small amount of the energy supplied by the laser. The amount of energy absorbed, while not significant, would heat the optical window causing localized thermal expansion, effectively creating another lens in the optical train. This alters the focal length of the system and drastically changes the energy density at the build plane. Given that builds often last several hours or days, progressive soot build up on the window leads to a gradual change in beam diameter and increase in porosity. Thermal lensing can be exacerbated due to disruptions in the gas flow; efficient gas recirculation is therefore critical to avoid soot build up.

In this work, the reasoning for emulating thermal lensing by changing the laser spot size was to enable creation of various types of porosity, at different levels of severity (Figure 2) in a controlled manner. The multi-phenomena process monitoring approach presented here is applicable to any situation where porosity-related flaws are liable to occur in LPBF. Thermal lensing is a challenging phenomenon and practically motivated from our ongoing work with highly regulated, safety-critical aerospace and nuclear industries. In these industries, manufacturers operate machines to the strictest quality standards and have established stringent standard operating procedures in place.

However, flaw formation often occurs despite extensive process optimization [44, 45]. Indeed, of all the multitude of possible failure modes identified by industry practitioners, soot build up on the optical window (through insufficient cleaning, clogged filter, long build times) was observed to be the most likely cause of process failures. Hence, despite established standard operating procedures, it is critical to certify, i.e., prove and document process quality, with in-situ data.

The second predominant reason for laser focus shift is observed in multi-laser systems. When two lasers are processing material in close proximity, the hot gas and vapor plume of one melt pool can cross the path of the other laser. The changes in density in the gas through which the laser passes causes refraction. This localized gradient of refractive index defocuses the beam and leads to a drop in energy density delivered to the powder bed. This effect can be potentially mitigated through pragmatic planning of the scan paths for each laser. While this work does not involve a multi-laser LPBF system, the presented approach can be scaled to such systems in the future.

In the literature, porosity of different types and severity is often created by changing the process parameters, such as laser power and velocity [23, 46]. However, such parameters studies are of marginal value to the industry, because, parameters are directly controlled and logged by an internal mechanism within the LPBF machine.

In contrast, stochastic variation in laser focus (laser spot size and height) is difficult to directly track in a production environment; a beam profiler cannot be installed on the powder bed during operation. Hence, for quality assurance purposes, cumbersome and expensive non-destructive examination with X-ray CT is currently required. Accordingly, there is substantial practical value in detecting laser focus issues earlier in the manufacturing process chain using in-process sensor data.

2.1.2 Build Plan and Test Parts

Experiments in this work were carried out on a Renishaw AM250 system using the manufacturer optimized parameters used shown in Table 1; these parameters were maintained constant for all specimens created in this work.

We emulated the deviation in laser focus by shifting the focal plane above and below the substrate as shown in Figure 2 (a1), (b1) and (c1). To mitigate the effect of part location on part quality [47], three separate experimental builds were conducted. Each build consisted of nine stainless steel 316L cylinders of Φ 5 mm and height 10 mm located at randomly assigned positions on the build plate. In total 27 cylinders were built in this work. The build locations for the parts on each build plate are shown in Figure 3 (a), (b), and (c). The center-to-center distance between the cylinders was 50 mm and a different laser focus height was set for each cylinder as shown in Figure 3. The laser focus height (L_{fh}) ranged from -20 mm to 12 mm in increments of 4 mm. The negative sign refers to the beam focused above the powder bed, whereas the positive sign implies the beam is focused below the powder bed. The focus height of 0 mm correlates to the beam converging on the surface of the powder bed.

Table 1: Constant processing conditions used to build the cylinders.

Process Parameters	Values [units]
Laser type and wavelength	200 W fiber laser, wavelength 1070 nm
Laser power, laser speed, point distance,	200 W, 750 mm·s ⁻¹ , 60 μm, 80 μs
exposure time for the bulk section	
Laser power, laser speed, point distance,	200 W, 444 mm·s ⁻¹ , 90 μs, 40 μm
exposure time for the inner border	
Laser power, laser speed, point distance,	110 W, 200 mm·s ⁻¹ , 100 μs, 20 μm
exposure time for the outer border	
Hatch spacing	110 μm
Layer thickness	50 μm
Scanning strategy	Meander-type scanning strategy with 67° rotation
Build atmosphere	Argon
Material type	Stainless Steel 316L
Powder size distribution	10-45 μm

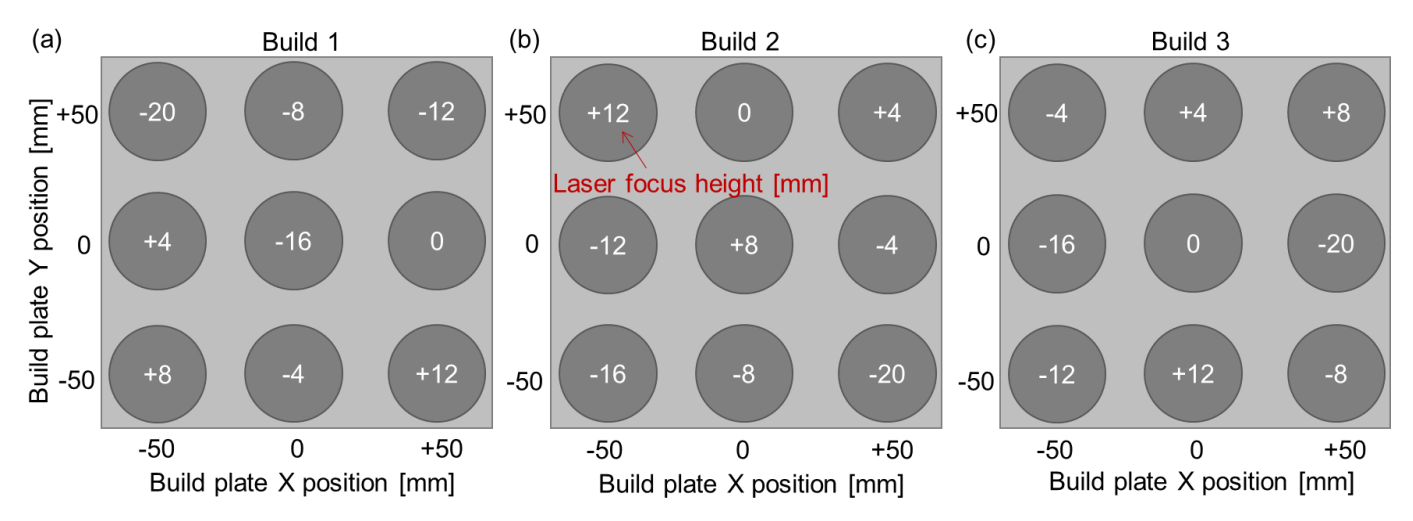


Figure 3: Build plate position of cylinders printed at different laser focus heights (L_{fh}) in (a) Build 1, (b) Build 2, and (c) Build 3. The position of cylinders across the three builds was randomized to account for the effect of position on part quality. The numbers indicate the L_{fh} , wherein the negative and positive values indicate that the laser is focused above and below the powder bed, respectively. $L_{fh} = 0$ mm caused the beam to converge on the powder bed.

Figure 4(a) tracks the effect of laser focus height (L_{fh}) on laser spot size (Φ_d). The laser spot size was measured using a dual slit laser beam profiler (Ophir Nanoscan 2). The laser spot size is quantified as the $1/e^2$ width of the Gaussian laser beam. From Figure 4, it is evident that the laser spot size decreases almost linearly as the laser focal plane is moved closer to the powder bed from above. The largest laser spot size ($\Phi_d = 421 \mu m$) corresponds to a $L_{fh} = -20 \mu m$ where the beam is considerably above the powder bed. Inversely, the smallest laser spot size ($\Phi_d = 63 \mu m$) was measured at the laser focus height of 0 mm, when the laser focal plane was on the powder bed.

The laser spot size increases again as the focal plane moves further below the powder bed beyond 0 mm laser focus height. While nearly identical spot size can be obtained at different laser focus height settings, the characteritics of the laser beam would be different. For example, a spot size of ~100 μ m is obtained at L_{fh} = -4 mm and L_{fh} = +4 mm. In the latter case (L_{fh} = +4 mm), the beam is focused below the powder bed and is converging, whereas in the former (L_{fh} = -4 mm) the

laser is focused above the powder bed and is diverging. A converging and diverging beam lead to drastically different porosity characterises as will be explained in Sec. 3.

Next, we analyzed the effect of laser spot size on energy density delivered to the powder bed. The traditional definition of energy density (E_v) [J·mm⁻³], shown in Eqn. (1), includes only the following processing parameters: laser power (P) [W], velocity (v) [mm·s⁻¹], hatch spacing (h) [mm], and layer thickness (t) [mm].

$$E_v = \frac{P}{v \times h \times t} \tag{1}$$

Since the foregoing process parameters are held constant (Table 1), in this work, the energy density is ~48.5 J·mm⁻³ for all specimens. Therefore, E_{ν} does not capture the effect of laser spot size. Other limitations of energy density in the context of LPBF have been noted by Bertoli *et al.* [48].

To overcome this drawback, we modified the energy density relationship from Eqn. (1) to include the laser spot size (Φ_d) [mm]. This modified relationship, shown in Eqn. (2), also encompasses the material properties of stainless steel 316L in the form of the thermal diffusivity term (α) [mm²·s⁻¹]. Thermal diffusivity is a function of the thermal conductivity (k), material density (ρ) , and specific heat (C_p) ; $\alpha = \frac{k}{\rho C_p} = 35000 \text{ mm}^2 \cdot \text{s}^{-1}$ at 1700 K.

The modified energy density definition in Eqn. (2) has units [W·mm⁻²], and is termed energy flux density E'_{ν} [33]. It quantifies energy flow per unit of area per unit of time.

$$E_{v}' = \frac{P}{v \times h \times t} \times \frac{\alpha}{\Phi_{d}}$$
 (2)

Figure 4 (b) tracks the energy flux density E'_v [W·mm⁻²] as a function of the laser focus height (L_{fh}) and laser spot size (Φ_d) . The highest energy flux density (E'_v) is realized when the laser is focused on the powder bed. As evident from Figure 4 (b), de-focusing the beam reduces the energy

flux density. A drawback with both E_v and E_v' is that they do not indicate if the beam is diverging or converging. In other words, the energy (flux) density does not have a positive or negative sign to indicate the position of the laser beam with respect to the powder bed. Therefore, the results in this work (Sec. 3) are presented in terms of laser focus height (L_{fh}) and laser spot size (Φ_d), and not energy flux density E_v' or energy density E_v .

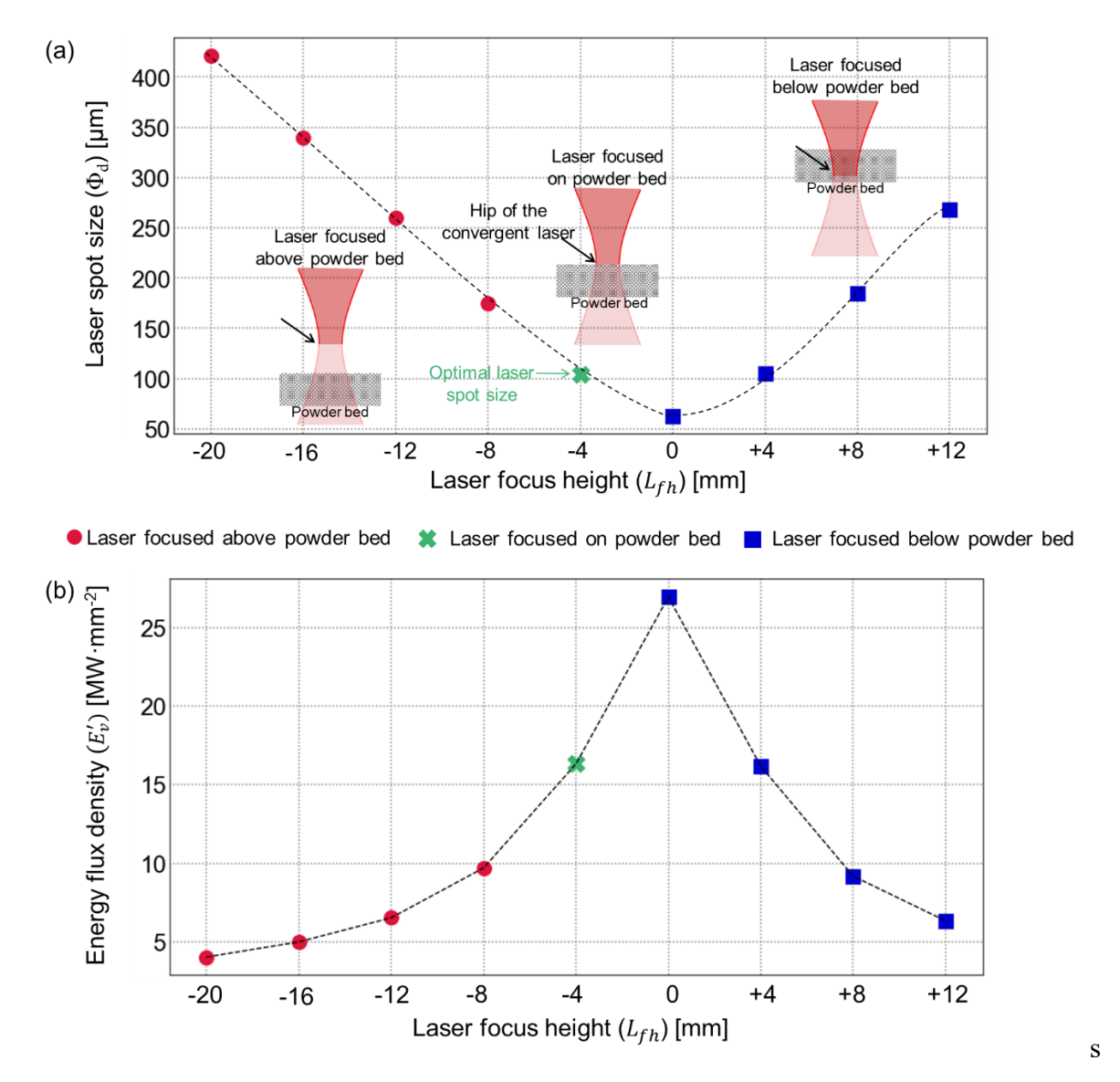


Figure 4: (a) Effect of laser focus height on laser spot size measured using a dual slit laser beam profiler. (b) Effect of laser focus height on energy flux density.

2.1.3 Materials Characterization

After processing, the parts were examined with non-destructive X-ray computed tomography (XCT) to quantify the effect of change in laser focus height on part porosity (Nikon XTH 225 ST at 10 µm/voxel resolution). The porosity was quantified using the VGSTUDIO MAX software native to the XCT machine. This analysis was further corroborated with Archimedes relative density measurements.

Next, the cylinders were cross-sectioned along the X-Y and X-Z (build direction) using electro-discharge machining. These cross-sections were then mechanically ground using SiC sandpaper of increasing grit size of 240, 360, 400, 600, 800 and 1200 µm, and finally polished to mirror finish using diamond paste of decreasing particle size of 3 µm, 1 µm, and 0.5 µm. The X-Y cross-sections of the cylinders were examined using optical microscopy to determine the type of porosity. Similarly, the effect of laser focus height on melt pool penetration depth was quantified by performing optical microscopy on the X-Z cross-sections of the cylinders.

2.2 In-process Monitoring

A schematic of the experimental setup is shown in Figure 5 (a). The sensing array consists of two high speed imaging cameras (Photron FASTCAM SA5) with bandpass optical filters of 700 nm and 950 nm at sampling rate of 100 kHz [29]. The resulting melt pool morphology data at the two wavelengths is exemplified in Figure 5 (b) and (c).

The temperature field (Figure 5 (d)) is obtained from the high-speed melt pool images captured at the two wavelengths. A detailed explanation of the procedure for obtaining the temperature field including the calibration of the measurements is described in Ref. [29]. To summarize, the operating principle is akin to imaging pyrometry. Consider the intensities of melt pool images acquired from Camera 1 and Camera 2 as $I_{\lambda 1}$ and $I_{\lambda 2}$, respectively. Planck's law states that the temperature of a

body (T) is proportional to the intensity of radiation (I_{λ}) , i.e., $T = \epsilon I_{\lambda}$, with emissivity (ϵ) as the proportionality constant. However, the emissivity is not constant, and depends on various factors including the temperature of the body and its surface finish.

Ratio pyrometry estimates the temperature (T) of the body by taking the ratio of the intensities measured at two different wavelengths $I_{\lambda 1}$ and $I_{\lambda 2}$ which has the effect of cancelling out the first-order emissivity term [23, 49]. The melt pool temperature measurements from this setup were subsequently calibrated with a known temperature source. The measurement error is ~5% at 1900K which further reduced at higher temperatures [29]. In this work, the high-speed images from Camera 1 (Figure 5 (b2)) were used to extract melt pool morphology (size, shape, and spatter) signatures. Each high-speed video image is of size 128 × 128 pixels with a spatial resolution of 25 μ m/pixel.

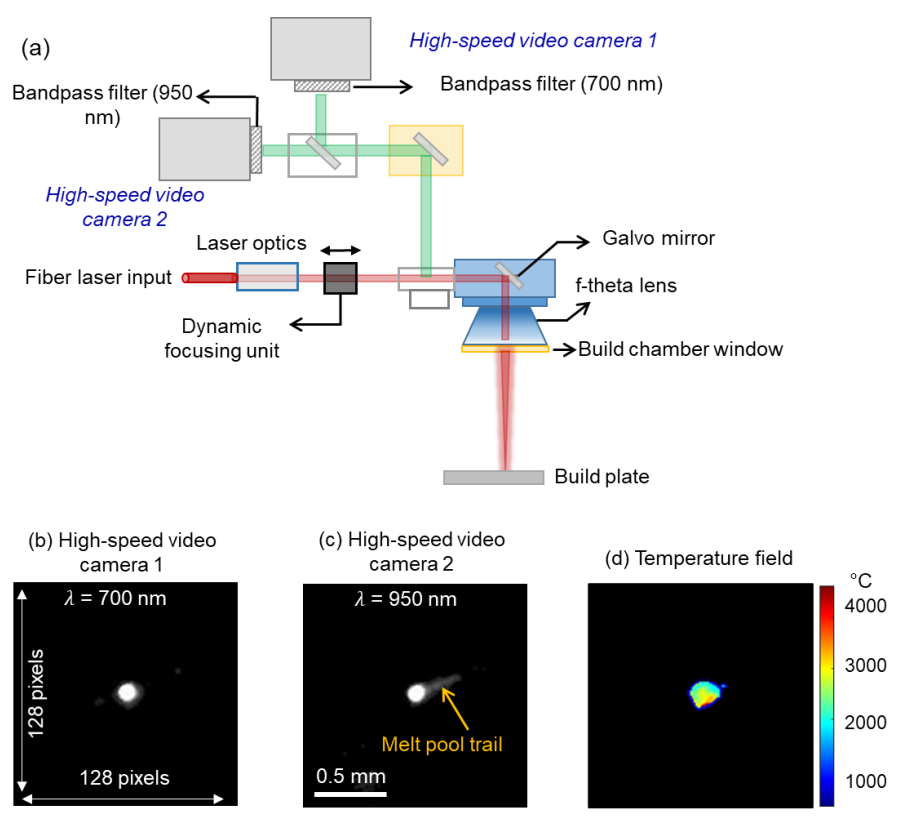


Figure 5: Schematic representation of the (a) two wavelength high-speed video camera sensing setup. (b) and (c) representative high-speed video camera frames collected at 700 nm and 950 nm, respectively. (d) is the temperature field image created from the high-speed video camera frames collected at the two wavelengths [29].

2.3 Extraction of physics-informed melt pool signatures from sensor data

In this work, three types of sensor signatures (features) were extracted from the sensor data as shown in Figure 6, these are: (i) morphology (shape and size) of the melt pool; (ii) characteristics (area, number, and intensity) of the spatter; and (iii) temperature distribution of the melt pool.

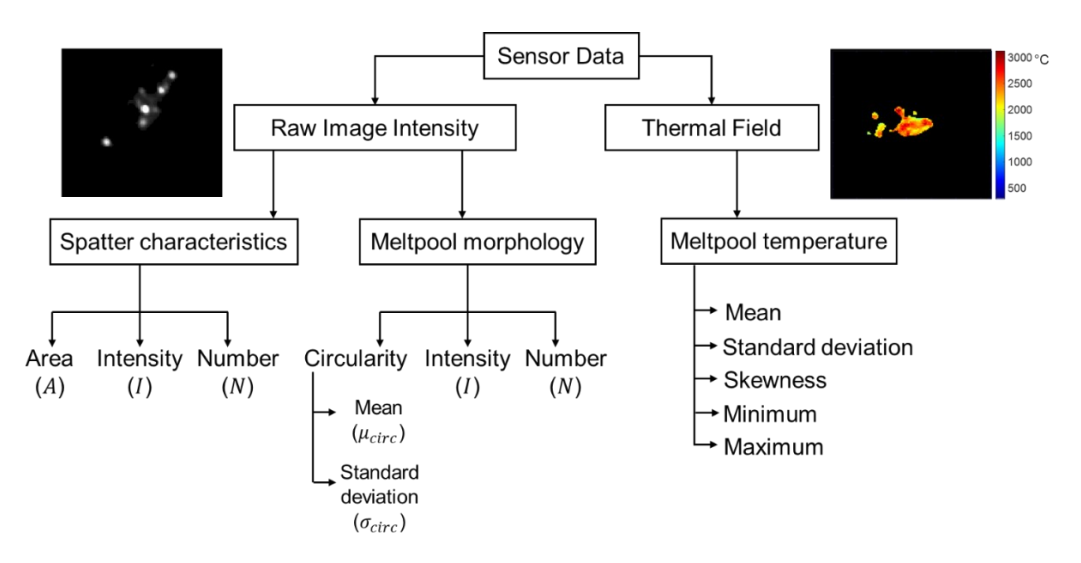


Figure 6: Schematic representation of the various physics-based features extracted from the different sensing modalities.

In the high-speed video camera images exemplified in Figure 7 (a), the melt pool consists of a body surrounded by spatter signatures, and plume-related features. To extract melt pool morphology, i.e., size, shape, and spatter, the k-means image segmentation algorithm was used to remove the plume-related noise from the high-speed images [50]. Figure 7 (b) shows the four clusters created by the k-means algorithm: background (Cluster 1), plume-related features (Cluster 2), spatter (Cluster 3), and melt pool (Cluster 4). Subsequently, 8 pixel-connectivity-based object detection algorithm was used to identify the various individual artifacts in the image. The k-means segmentation algorithm is available as Python scripts and are capable of rapid deployment with minimal computational expense.

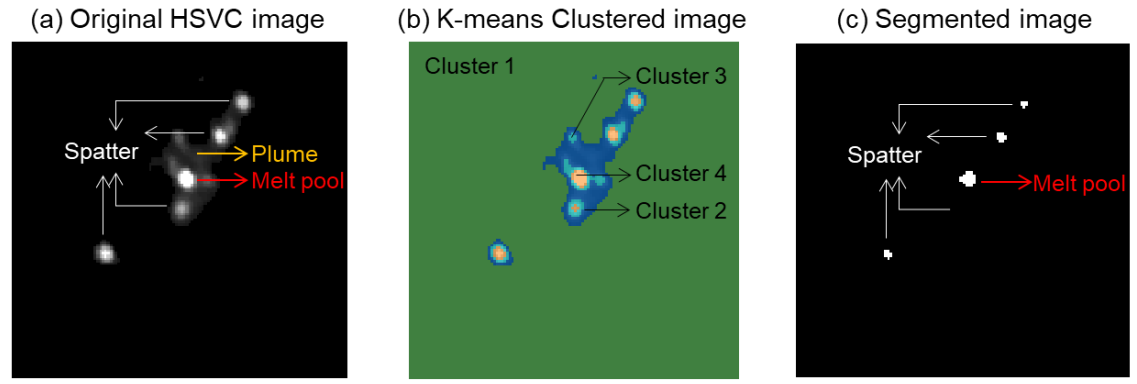


Figure 7: Approach followed to segment high-speed video camera images. (a) Sample high-speed video camera image is segmented into 4 clusters using k-means clustering as shown in (b). (c) Segmented image in which only pixels from Cluster 4, i.e., the brightest pixels are retained.

These pre-processed images (Figure 7 (c)) were analyzed to extract melt pool morphology characteristics. Each pre-processed image was divided into five regions (W1 - W5) as shown in Figure 8 (a). The rationale is that the melt pool is located in the center region (W5), while the spatter is captured in the surrounding regions (W1-W4). The regions W1-W4 are each 64×64 pixels and the central region W5 is 25×25 pixels.

From the four non-central regions (W1 – W4), three features were extracted; area (A), intensity (I), and number (N) of melt pool and spatter artifacts contained in the region. The area of an artifact is given as $A = \pi \times L_{major} \times L_{minor}$, where L_{major} and L_{minor} are the lengths of major and minor axes of ellipse fit to the artifact as shown in Figure 8€. This feature provides information about the size of the artifacts present in a region. The intensity of an artifact is mathematically formulated as $I = \sum_{p=1}^{p} I_p$, where I_p is the grey value of pixel p in the artifact, and p is the total number of pixels in the artifact. The feature N quantifies the number of artifacts in a region.

Researchers have shown that spatter formation has a significant effect on porosity formation in LPBF parts [34, 51-54]. Using high-speed imaging Nassar *et al.* [51] observed that spatter formation was caused due to the inelastic collision between near and far away particles ejected from the melt

pool, and the amalgamation of partially sintered particles. The authors confirmed the formation of lack-of-fusion porosity due to spatter formation via scanning electron micrography.

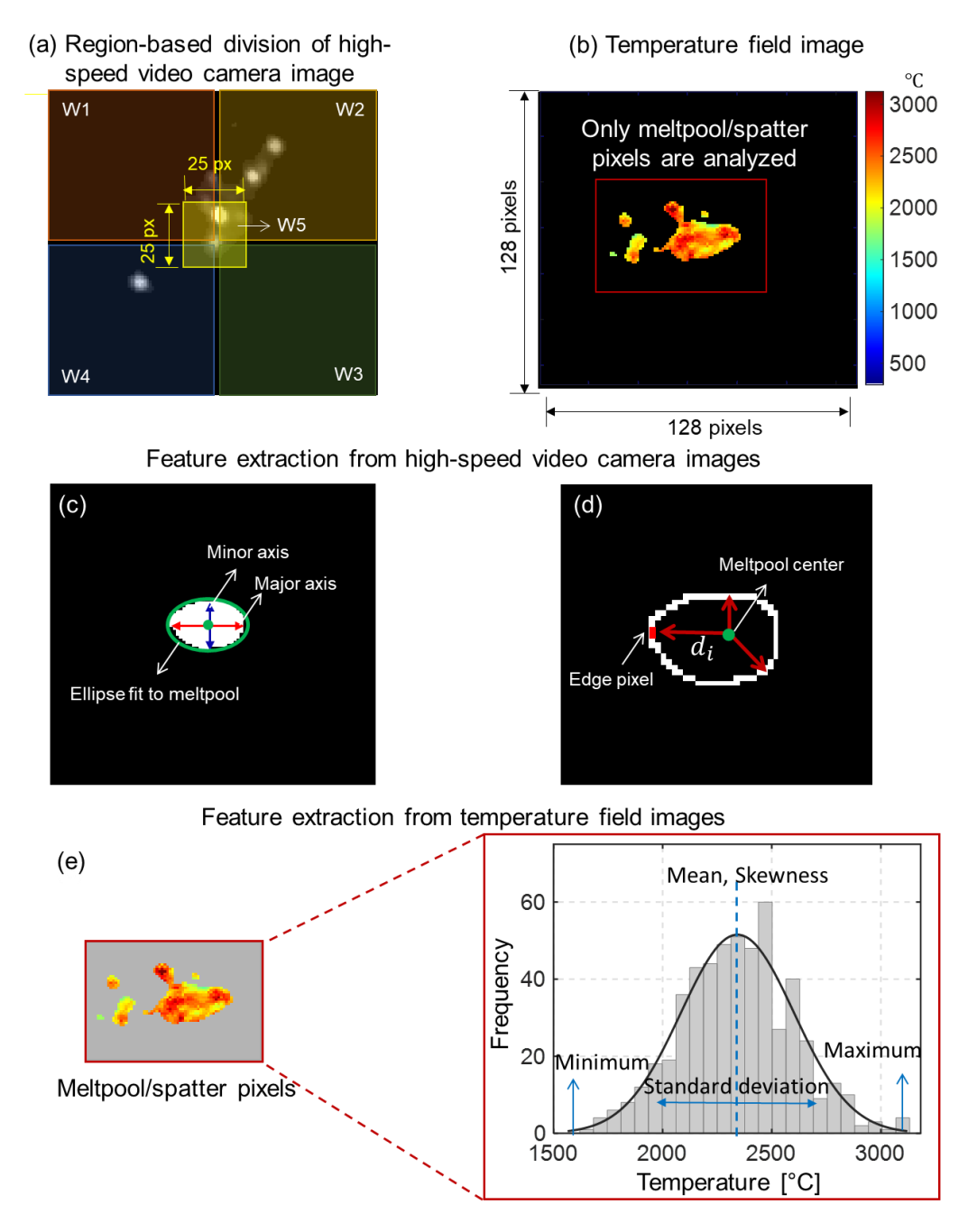


Figure 8: Sample in-process sensor data used for feature extraction. (a) High-speed video camera images are divided into 5 windows as shown above. (b) Pixels belonging to melt pool, and spatter (highlighted) were used for feature extraction. (c) Melt pool size was determined by fitting an ellipse to it and using its axes lengths. (d) Melt pool circularity was calculated by taking a mean and standard deviation of the distance of melt pool center from its edge pixel \in (e) Melt pool and spatter pixels extracted from temperature field images, and the statistical features extracted from them.

Esmaeilizadeh et al. [53] compared the quality of parts sintered on virgin powder and spatter-rich regions of the powder bed. X-ray computed tomography analysis showed that the spatter-rich region depicted high levels of porosity compared to those printed on virgin powder. The role of spatter in creating flaws is further confirmed in the recent work of Qiu et al. [54]. The authors established the correlation between porosity and spatter formation with the help of high-speed imaging and computational fluid dynamics modelling. Repossini et al. [34] demonstrated that spatter signatures are effective for process monitoring in LPBF. The authors extracted statistical features of the spatter signatures and used them in a regression model to detect the onset of porosity.

The importance of tracking spatter particles in the context of this work is evident on examining high-speed video images in Figure 9. These images are acquired with a monochrome camera sampling at 10 kHz integrated co-axial to the laser path in our apparatus; this sensor was not used in the current work since it acquires data over a short burst, not over the entire build. A sample video acquired when the laser was out of focus is given in Appendix C (Video C.1). The sequence of images shown in Figure 9 (a) track a spatter particle that has traveled ahead of the laser path, and ultimately settled on un-melted powder within the boundary of the part. On subsequent passes of the laser, this spatter particle is liable to impede complete melting of the powder. Likewise, in Figure 9 (b) several spatter particles have settled on previously melted regions of the part. These spatter particles are liable to interfere with deposition, as well as melting of powder on subsequent layers. Based on prior works in the literature and the observation of spatter (Figure 9), spatter characteristics, such as area, intensity, and number were extracted from the high-speed video camera data, and subsequently used for process monitoring.

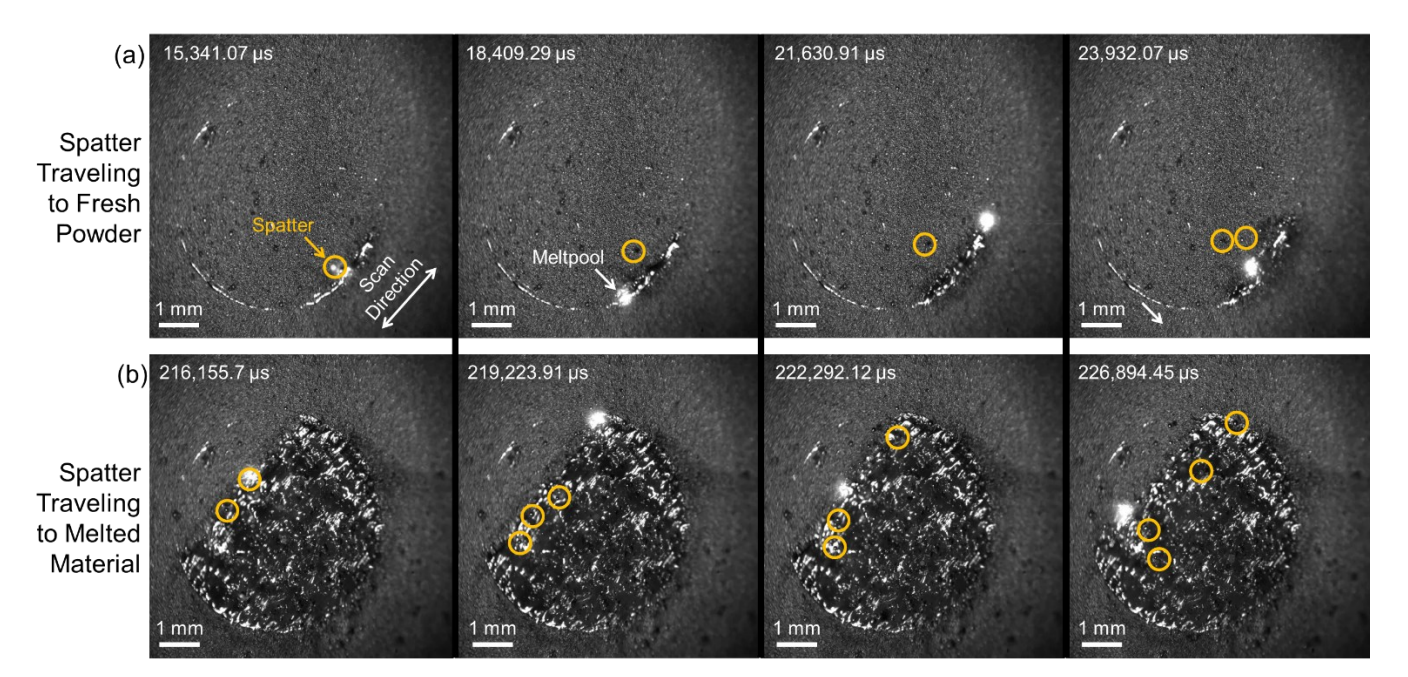


Figure 9: (a) Example from high-speed video imaging showing ejection of spatter particles that has landed onto un-melted powder within the boundary of the part. (b) spatter particles also land onto previously melted material within the part boundary. The video from which this image sequence was extracted is given in Appendix C, Video C.1.

From the fifth region (W5), placed centrally in the image shown in Figure 8, two additional features were extracted, namely, mean, and standard deviation of the circularity of the melt pool. These features capture the size and shape of the melt pool [55]. The mathematical representation of mean μ_{circ} and standard deviation σ_{circ} of circularity of the melt pool is given in Eqn. (3).

$$\mu_{circ} = \frac{1}{N_{edge}} \sum_{i=1}^{N_{edge}} d_i$$
 (3)

$$\sigma_{circ} = \sqrt{\frac{\sum_{i=1}^{N_{edge}} (d_i - \mu_{circ})^2}{N_{edge}}}$$

Here N_{edge} is the number of edge pixels of the melt pool, and d_y is the Euclidean distance from the center of the melt pool to an edge pixel as shown in Figure 8(d). To elaborate, the mean circularity (μ_{circ}) is representative of the melt pool size, and the standard deviation (σ_{circ}) of circularity captures the melt pool shape (uniformity).

Prior works have established that melt pool morphology (shape and size) has a significant effect on part porosity. For instance, Khairallah *et al.* [19] established that penetration is low at high laser velocities, thereby leading to balling. This balling effect was indicative of partial fusion of the powder particles which ultimately leads to severe lack-of-fusion porosity. Guo *et al.* [39] studied the variation in melt pool dimensions (length, width, and depth) using in-process high-speed X-ray imaging. It was observed that under low energy density conditions the melt pool dimensions were extremely small resulting in impartial fusion of powder particles and eventually lack-of-fusion porosity. Similar observations regarding the melt pool behavior under low energy density conditions were made by Li *et al.* [56] using a volume of fluid-based three phase model. Based on these prior research works, the melt pool morphological features in terms of its circularity were used in this work.

Lastly, from the melt pool temperature field images (Figure 8(b)), the following low-level statistical features were extracted: mean, standard deviation, skewness, minimum, and maximum of temperature values. These features were extracted to encapsulate the temperature distribution of the melt pool region.

2.4 Machine Learning Algorithms

Two machine learning tasks were undertaken in this work as summarized in Table 2. The aim of Task 1 is to detect systematic drift in the laser focus by classifying the laser spot size as a function of the physics-based process signatures described in Sec. 2.3. The idea is to notify the operator of an impending shift in laser spot size so that an appropriate corrective action can be taken.

Task 2 consists of distinguishing the type of porosity using the extracted sensor signatures. As it will be elucidated further in Sec. 3.1, the following regimes of porosity are observed from the materials characterization analysis: (i) severe lack-of-fusion porosity, (ii) lack-of-fusion porosity,

(iii) negligible (optimal) porosity, and (iv) keyhole porosity. To avoid confounding, we did not use melt pool images from the contour region in our machine learning analysis; only meltpool images from the bulk part were used.

Table 2: Different levels at which the laser spot size was classified in this work.

Task 1 – Determine laser spot size deviation		
Classification levels	Laser spot size (Φ _d) [μm]	
9-way	421 vs. 340 vs. 260 vs. 175 vs. 104 (optimal) vs. 63 vs. 105 vs. 185 vs. 268	
Task 2 – Determine type of porosity		
Classification levels	Porosity type	
4-way	Severe lack-of-fusion vs. lack-of-fusion vs. optimal vs. keyhole	

2.4.1 Model types and characteristics

Researchers have primarily used two approaches for machine learning-based monitoring: (i) feature-driven, and (ii) raw data-driven. To elaborate, feature-based machine learning approaches contain characteristics of the in-process sensor data, such as melt pool size and temperature which are subsequently used as inputs in machine learning models. In contrast, raw data-driven approaches use unprocessed in-process sensor data directly with deep learning models. In this work, the feature-driven and raw data-driven machine learning models were compared.

In feature-driven machine learning approaches the sensor signatures described in Sec. 2.3 are used as inputs to different machine learning models, namely, support vector machines (SVM), multilayer perceptron (MLP), k-nearest neighbors (KNN), and random forest (RF) [57-60]. The melt pool morphology and spatter characteristics, and temperature distribution features were used together and separately as inputs to the various machine learning models to predict drift in laser spot size and porosity.

On the other hand, the raw data-based monitoring approaches rely on deep learning models to extract features implicitly and predict flaw formation or process drifts. Some of the widely used deep

learning models are convolutional neural networks (CNN) [61-67], recurrent neural networks [68-71], generative adversarial neural networks [72, 73], and autoencoders [74, 75]. In this work, a CNN was used as the representative deep learning model. While the CNN can learn complex relationships, the large number of learnable parameters (>200,000) to tune the CNN make it intractable and difficult to interpret. A summary of the CNN architecture is provided in Figure 10. Similar CNN models have been implemented in our previous works [55, 76].

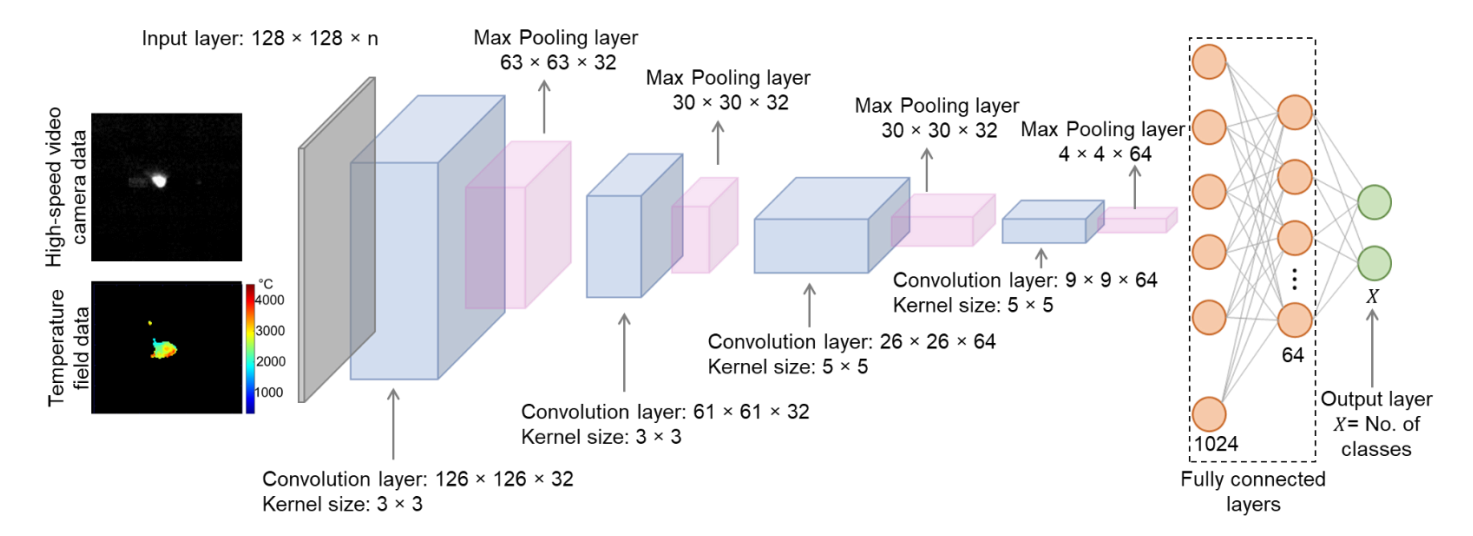


Figure 10: The architecture of the convolutional neural network (CNN) used in this work.

Despite demonstrated success in recent additive manufacturing literature, the complexity and lack of interpretability of deep learning models hampers their ability to transferability across different part shapes and materials [55, 74]. These black-box deep learning models provide no physical insight into the features extracted from the sensor data and hence cannot be related to the process physics. Furthermore, the deep learning models are computationally intensive and require extensive input-output labeled data for training.

In addition to simple machine learning and deep learning models, we also evaluated conventional statistical models that do not include any active learning step. The statistical models used were the ridge regression-based classifier (RRC) and the nonlinear logistic regression classifier

(NLR). The subpar performance of these models indeed motivated the use of machine learning models.

A summary of the parameters used in the machine learning models is reported in Table 3. A preliminary assessment of the performance of the models tested in this work was evaluated in terms of the F1-score as it considers both the Type I (false alarm or false positive) error and the Type II (failing to detect or false negative) error [77]. The false positive rate (FPR, Type I error rate) and false negative rate (FNR, Type II error rate) were also used as a metric to compare the various models. In addition, the receiver operating characteristic (ROC) curves and area under the curve (AUC) were used for further quantitative analysis of the prediction performance of the machine learning models.

Table 3: Summary of the hyperparameters used in various machine learning models.

Machine learning model	Summary
Support Vector Machine (SVM)	- Soft margin classifier
	- Nonlinear kernel: Radial basis
	- L2 Regularization
Multilayer perceptron (MLP)	- Number of hidden layers = 1
	- Number of neurons = Based on classification task's
	complexity
	- Activate function = ReLU
	- Batch size = 200
	- Learning rate = 0.001
	- L2 Regularization
Random Forest (RF)	- Number of trees = Based on classification task's complexity
	- Spilt criterion = Gini impurity
	- Bootstrap samples = 80%
	- Maximum features used at each split = (number of input
	features) ^{1/2}
K-nearest neighbors (KNN)	- Number of neighbors = Based on classification task's
	complexity
	- Weighting function = inverse distance
	- Distance metric = Manhattan or Euclidean distance (based
	on classification task's complexity)

2.4.2 Model training and testing

For predicting deviation in laser spot size (Task 1), approximately 12,000 data points (sensor signatures) for each of the 9 classes were used (108,000 total input vectors). The dataset was first spilt into training and testing subsets, wherein 65% of the data (7800 data points per class; 70,200 total) was used for training, and the remainder 35% of the data (4200 per class; 37800 total) were isolated for testing. The machine learning models results presented in this work are based on the testing dataset which is unseen by the trained models. An identical training and testing procedure was applied for the 4-class porosity classification study (Task 2) with the exception that 6,000 data points were used per class with 65% (3900 data points per class) for training, and 35% (2100 data points per class) for testing.

The training dataset was used for hyperparameter optimization for the various machine learning models. For the hyperparameter training, a 10-fold cross-validation technique was used [78]. The hyperparameter optimization used a sequential Bayesian hyperparameter optimization approach to avoid the combinatorial grid-search method which is time consuming and computationally intensive [79].

3 Results

This section is organized as follows. In Sec. 3.1, we quantify the effect of change in laser spot size (Φ_d) on type and severity of porosity. The effect of laser spot size on melt pool penetration depth is provided in Sec. 3.2. In Sec. 3.3, we correlate the melt pool morphology and temperature field with varying laser spot size and porosity. Finally, in Sec. 3.4 we use the features extracted from high-speed video camera and temperature field images to predict the deviation in laser spot size (machine learning Task 1) and the type of porosity (machine learning Task 2).

3.1 Effect of laser spot size on porosity

3.1.1 Severity of porosity from X-ray CT analysis and Archimedes relative density

Nondestructive X-ray CT (XCT) analysis was used to quantify the effect of laser spot size on severity of porosity in terms of the defect volume ratio (DVR). The DVR is the ratio of the volume of voids present in a sample and the volume of the total sample; it is obtained from the VGSTUDIO MAX software. Additionally, the samples were subjected to the conventional Archimedes relative density measurements.

Figure 11 (a) depicts the change in DVR and Archimedes relative density as a function of varying laser spot sizes. The DVR ranges from 0% to 2% and the corresponding relative density ranges from 98% to 90%. It was observed that build position (location) did not have a significant effect on porosity. For example, for the cylinders that were built with laser in-focus (nominal condition), i.e., the laser was focused on the build plate ($L_{fh} = 0$ mm), resulted in porosity with standard deviation of 0.07% across the three builds. Thus, confirming that laser focus height (or laser spot size) has a more pronounced effect on porosity in comparison to part location on the build plate.

Cylinders built with the laser focused above the substrate (Φ_d = 421 µm, L_{fh} = -20 mm to Φ_d = 175 µm, L_{fh} = -8 mm) have higher DVR (more porosity) in comparison to the cylinders built with laser focused below the substrate. As will be evident from the optical microscopy analysis described in the forthcoming section (Sec. 3.1.2), severe lack-of-fusion porosity was observed when the laser was focused above the powder bed. When the laser was focused at or slightly below the powder bed, the energy density was sufficient to increase the amount of keyhole porosity. Cylinders with keyhole porosity have a low DVR (high density) because they typically have a smaller diameter in comparison to lack-of-fusion pores. These observations are confirmed from the XCT images in the X-Y plane shown in Figure 11 (b1), (c1) and (d1).

Figure 11 (b2), (c2), and (d2) show X-Z plane XCT slices of the cylinder built with the laser focus height of -20 mm, -16 mm, and -12 mm resulting in laser spot size of Φ_d = 421 μ m, Φ_d = 340 μ m, and Φ_d = 260 μ m, respectively. It is apparent that the lack-of-fusion porosity transcends the X-Y plane and is present across layers in the X-Z plane as well. Therefore, the poor hatch fusion within a layer, is compounded by poor fusion between multiple layers.

3.1.2 Type of porosity from optical microscopy

The cylinders were characterized using optical microscopy to determine the type of porosity formed as a result of changing laser spot size. Figure 12 shows the X-Y plane optical micrographs of the cylinders. The cylinders built with the laser focused above the substrate (L_{fh} = -12 mm to L_{fh} = -20 mm), resulting in corresponding laser spot size of Φ_d = 260 μ m to Φ_d = 421 μ m, exhibit severe lack-of-fusion porosity. Instances of balling are also observed along the contour of these specimens. The severe lack-of-fusion flaws can be attributed to the reduction in the applied energy density as the laser beam is spread over a larger area [41, 55, 80]. The lack-of-fusion porosity is mitigated as the laser focal plane approaches the substrate.

Cylinders that were built with the laser focused at or slightly below the substrate ($L_{fh} = 0$ mm to $L_{fh} = +8$ mm) exhibit keyhole porosity due to the excessive applied energy density [19, 33, 43]. Further shifting the laser focal plane below the substrate reintroduces lack-of-fusion porosity as the powder is not sufficiently melted. For example, the cylinder built at $L_{fh} = +12$ mm exhibits an onset of lack-of-fusion porosity as the laser beam is again spread over a larger area.

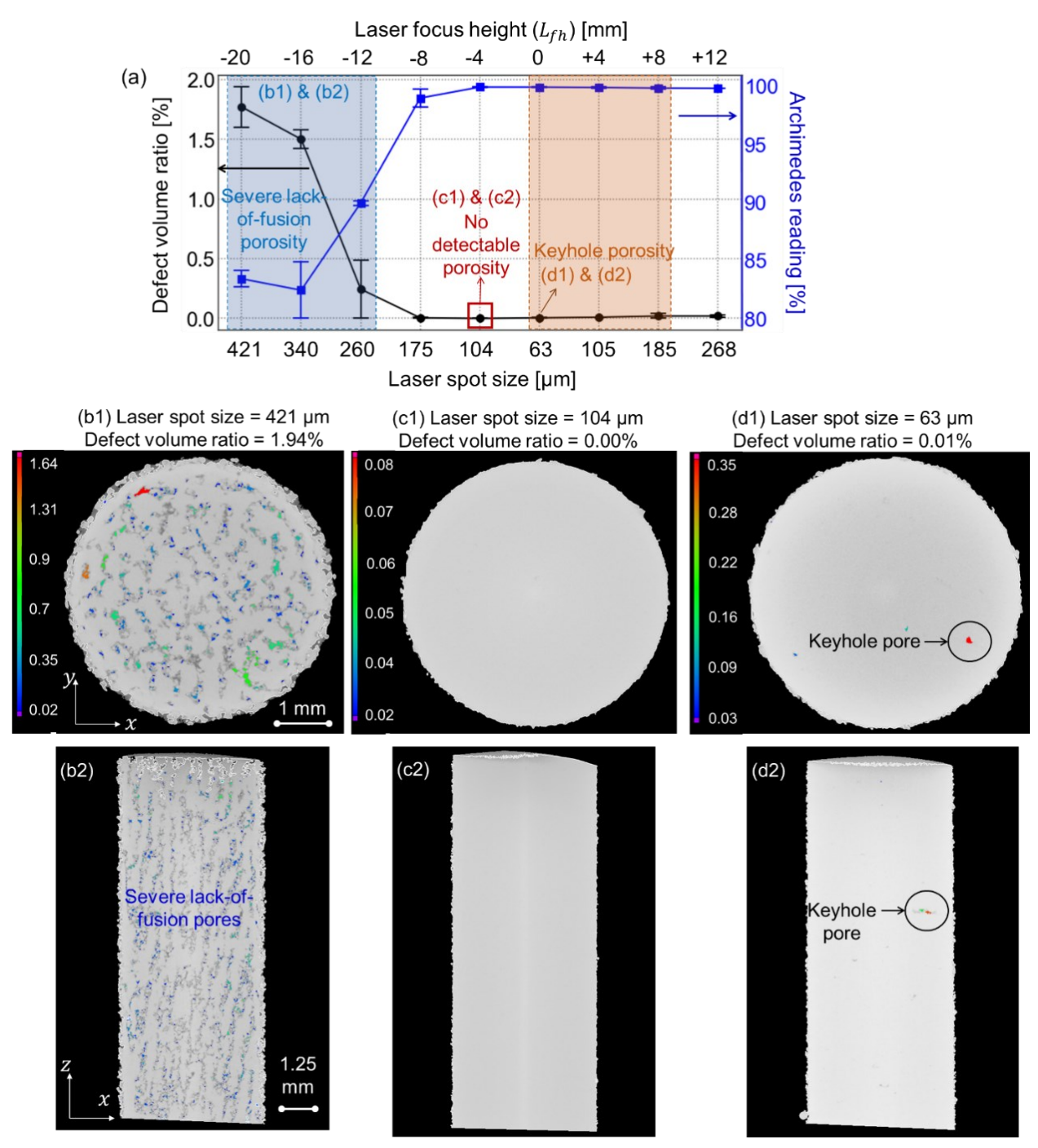


Figure 11: Effect of laser spot size on type of porosity and pore severity. Results of the X-ray computed tomography (XCT) of the cylinders. (a) Defect to volume ratio (DVR) and Archimedes density of the cylinders built under varying laser spot size, and laser focus height. (b1) and (b2) are the XCT images of the cylinder built at 421 μ m laser spot size (highest DVR) in the X-Y and X-Z planes, respectively showing severe lack-of-fusion porosity. (c1) and (c2) are the XCT images of the cylinder built at 104 μ m laser spot size (ideal) in the X-Y and X-Z planes, respectively. (d1) and (d2) are the XCT images of the cylinder built at 63 μ m laser spot size in the X-Y and X-Z planes, respectively. Color bars are the pore diameters in mm.

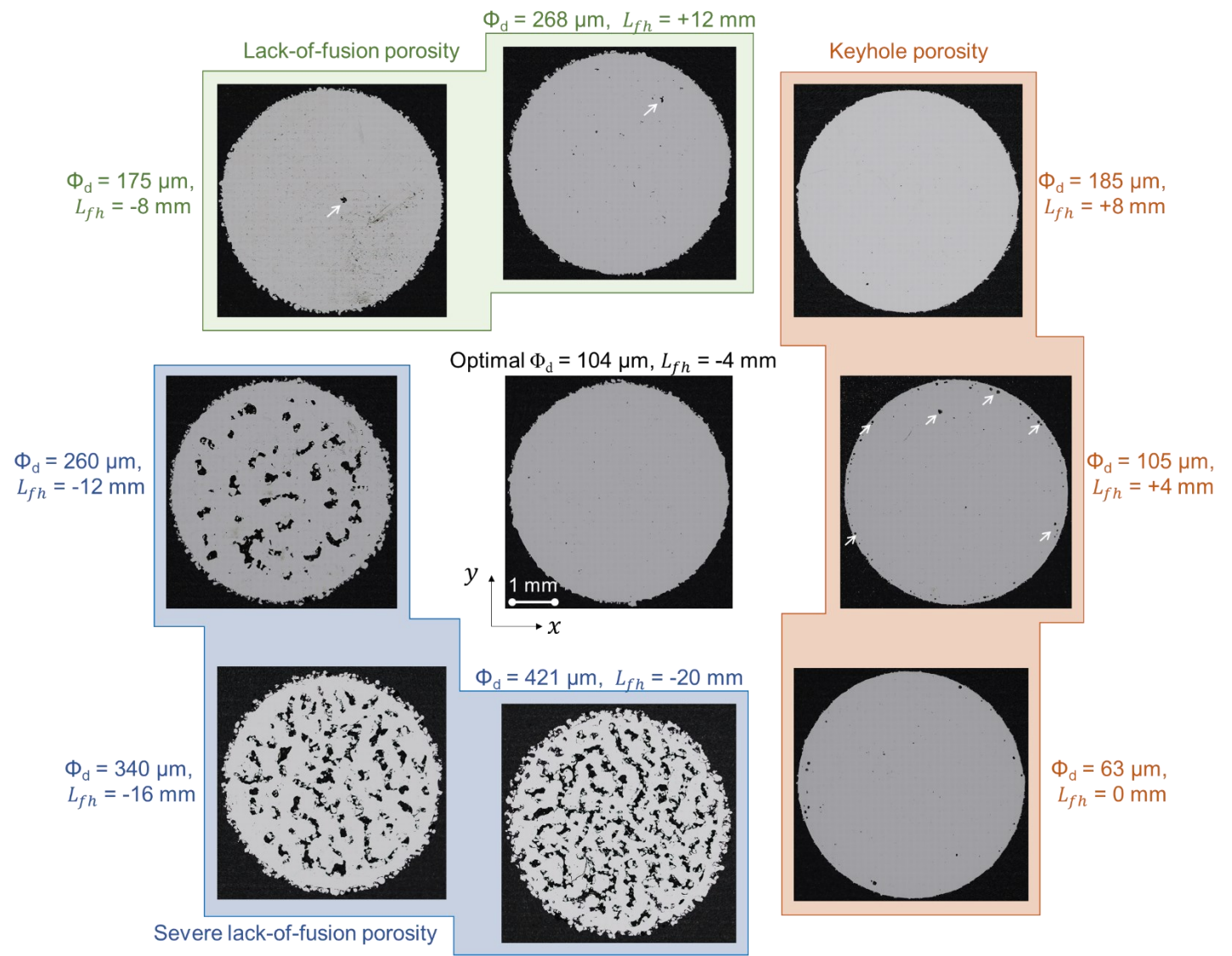


Figure 12: Effect of laser spot size on type of porosity and pore severity. Optical micrographs of cylinders in the X-Y plane built under different laser focus heights. Cylinders that were built at laser focus height above the substrate (-20 mm to -8 mm) exhibit severe lack-of-fusion porosity and balling on the contours (highlighted in light blue color). Cylinders that were built at laser focus height below the substrate (0 mm to +12 mm) keyholing porosity (highlighted in peach color). Lowest amount of porosity is seen in the cylinder built at the optimal laser focus height of -4 mm.

3.2 Effect of laser spot size on melt pool penetration depth

The X-Z cross-sections of the cylinders were polished and etched using Adler's reagent. Figure 13 shows the representative optical micrographs of cylinders built at varying laser spot sizes. Etching the parts reveals the effect of laser spot size on the melt pool penetration and characteristics of pore formation.

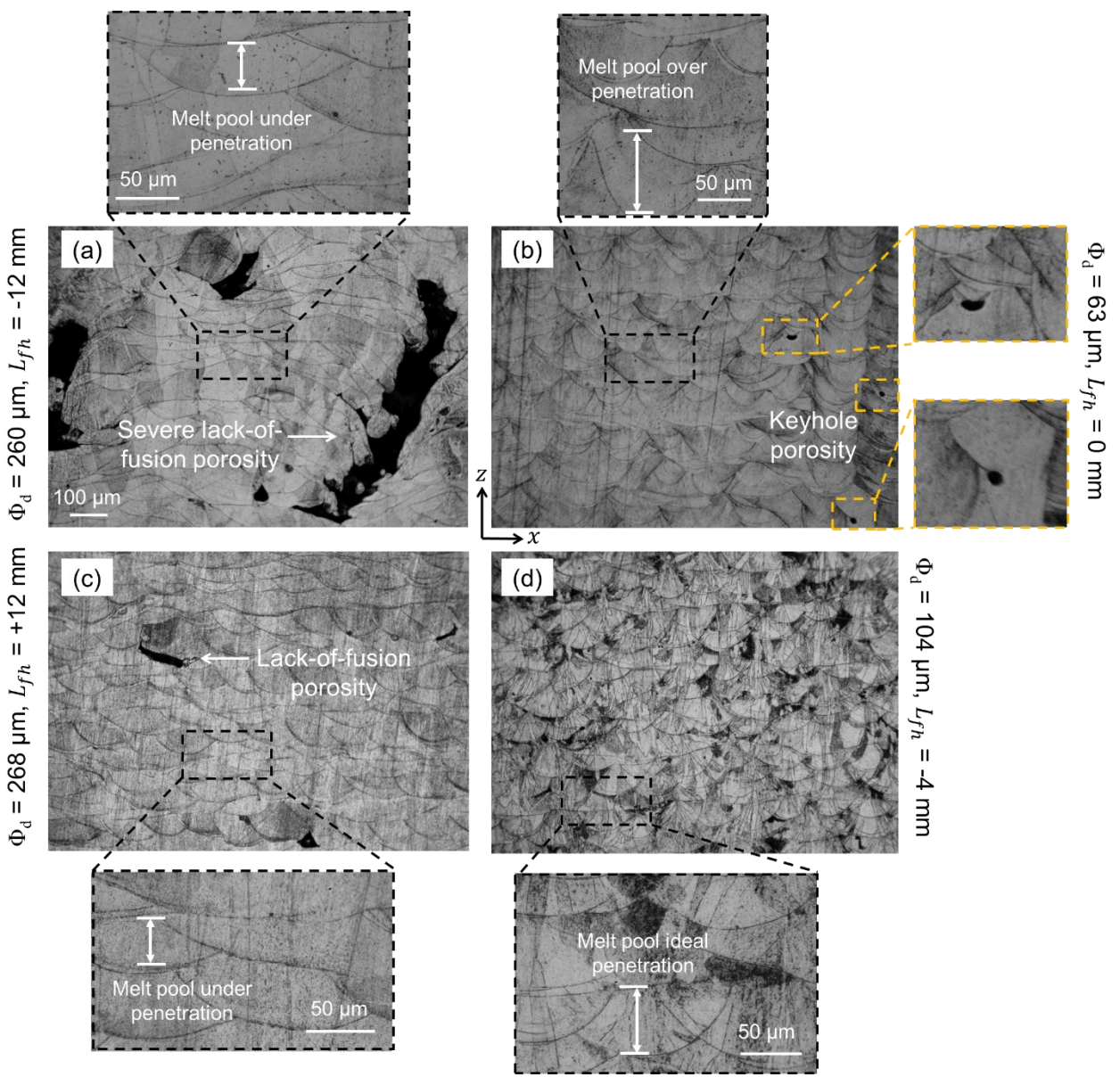


Figure 13: Effect of laser spot size on meltpool penetration. X-Z plane optical micrographs of cylinders deposited at (a) 260 μ m, (b) 63 μ m, (c) 268 μ m, and (d) 104 μ m. Melt pool penetration depth is observed to significantly vary with laser spot size. Φ_d = laser spot size, L_{fh} = laser focus height.

Figure 13 (a) and (c) show that laser spot size of ~260 μ m results in low melt pool penetration depth and is correlated to lack-of-fusion porosity. Contrarily, when the laser spot size is significantly reduced to 63 μ m ($L_{fh} = 0$ mm), a drastic increase in melt pool penetration is observed as shown in Figure 13 (b). This over penetration of the melt pool eventually leads to keyhole porosity, as demarcated with dark yellow boxes in Figure 13 (b). Ideal melt pool penetration depth is observed when the laser spot size is maintained at $\Phi_d \sim 104$ μ m corresponding to $L_{fh} = -4$ mm (Figure 13 (d)). Accordingly, the cylinders deposited at this laser spot size exhibit no porosity.

3.3 Effect of laser spot size on melt pool signatures

3.3.1 Melt pool morphology and spatter characteristics

It is established from previous works that change in applied energy density and part geometry influences the melt pool and spatter characteristics in LPBF [23, 55, 81-83]. The high-speed camera frames (Figure 14) were analyzed to quantify the effect of change in laser spot size on melt pool and spatter in terms of their size, shape, frequency, and location.

When the laser is focused slightly above the powder bed ($\Phi_d = 104 \mu m$, $L_{fh} = -4 \text{ mm}$), the melt pool has a near-circular shape with minimal spatter (Video A.2, Appendix A). On the contrary, when the laser was focused considerably below the powder bed, i.e., $L_{fh} = +12 \text{ mm}$, prominent spatter artifacts were observed (Video A.4, Appendix A); this operating region corresponds to lack-of-fusion porosity.

In the region where keyhole formation was observed, i.e., $L_{fh} = 0$ mm (Video A.3, Appendix A), $L_{fh} = +4$ mm, and $L_{fh} = +8$ mm, the melt pool is relatively compact with reduced spatter. In contrast, when the laser was focused above the substrate ($L_{fh} = -8$ mm to $L_{fh} = -20$ mm), wherein severe lack-of-fusion was observed apart from significant presence of spatter, the melt pool size is

relatively diffuse and ill-defined (especially at L_{fh} = -16 mm and L_{fh} = -20 mm). A sample high-speed video acquired at L_{fh} = -20 mm is given in Appendix A (Video A.1).

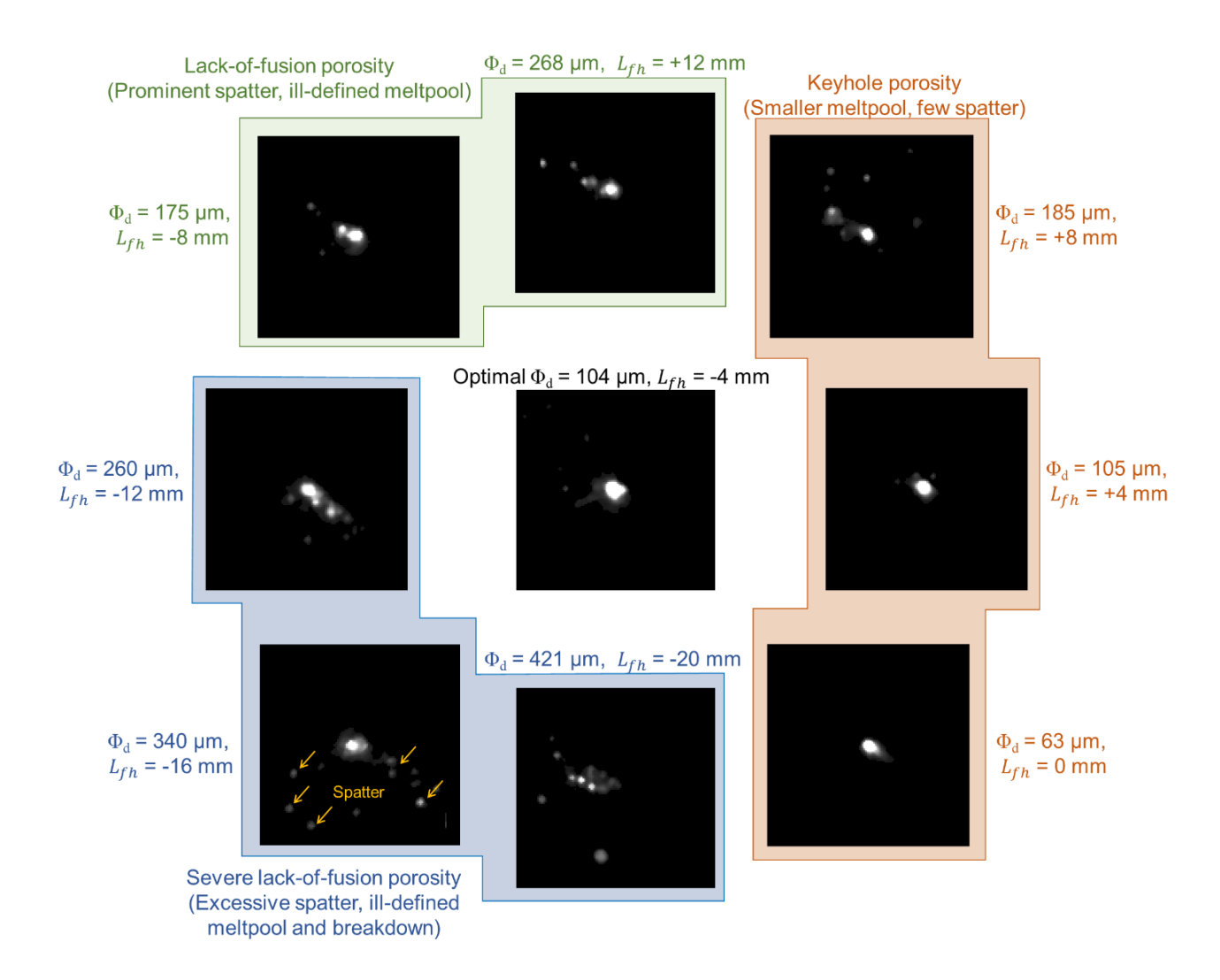


Figure 14: Representative high-speed video camera frames collected while building cylinders under varying laser spot sizes (Φ_d) and laser focus height (L_{fh}). Sample high-speed videos from the four above-shown regimes, viz. severe lack-of-fusion porosity, keyhole porosity, optimal porosity, and lack-of-fusion porosity, are given Appendix A.

The foregoing visual observations are quantified in Figure 15 (a) and (b), where the melt pool area (A) and number of spatter artifacts (N) is tracked as a function of the laser spot size, respectively. Both these features show similar non-linear behavior with respect to the laser spot size. For example, in Figure 15 (a), when the laser is focused above the powder bed $(L_{fh} = -12 \text{ mm})$ to $L_{fh} = -20 \text{ mm}$)

the melt pool area (A) is nearly 100 pixels² compared to 30 pixels² at the optimal setting ($L_{fh} = -4$ mm). As the laser is focused under the powder bed for $L_{fh} = 0$ mm, the melt pool area reduces to less than 20 pixels² corresponding to keyhole formation. However, when the laser is focused shifted further below the powder bed, the size of the melt pool increases again as the beam is spread out.

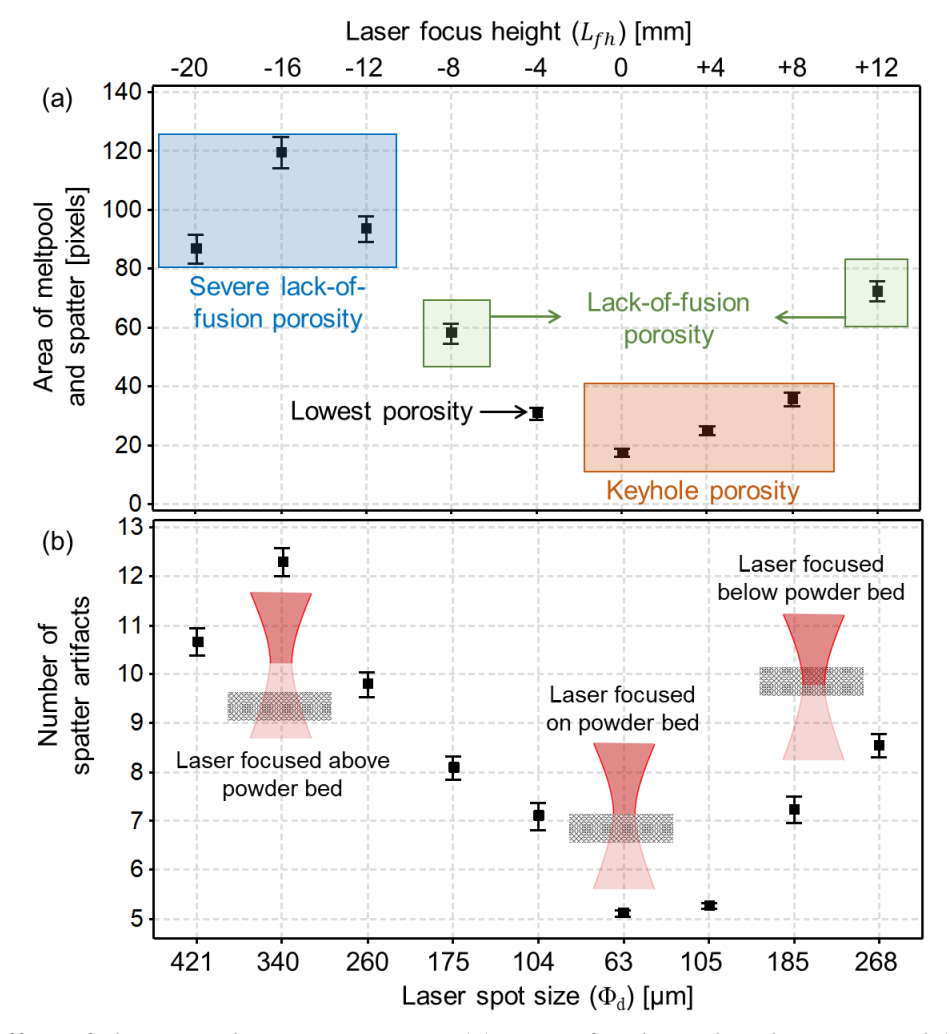


Figure 15: Effect of change in laser spot size on (a) area of melt pool and spatter and (b) number of occurrences of artifacts in high-speed video camera images. Error bar is 1 standard deviation, and 1000 samples were used.

3.3.2 Melt pool temperature distribution

The effect of laser spot size on melt pool temperature is summarized in Figure 16. It is evident from visual comparison that the melt pool temperature is relatively lower when the laser is focused

above the powder bed (L_{fh} = -12 mm to L_{fh} = -20 mm) compared to when it is focused below the powder bed (L_{fh} = 0 mm to L_{fh} = +8 mm). These correspond to lack-of-fusion and keyhole formation, respectively. Sample temperature field videos acquired at L_{fh} = -20 mm and L_{fh} = 0 mm are given in Appendix B as Video B.1 and Video B.3, respectively. The mean melt pool temperature is again reduced when the laser beam is focused considerably below the powder bed (Φ_{d} = 268 μ m, L_{fh} = +12 mm) (Video B.4, Appendix B).

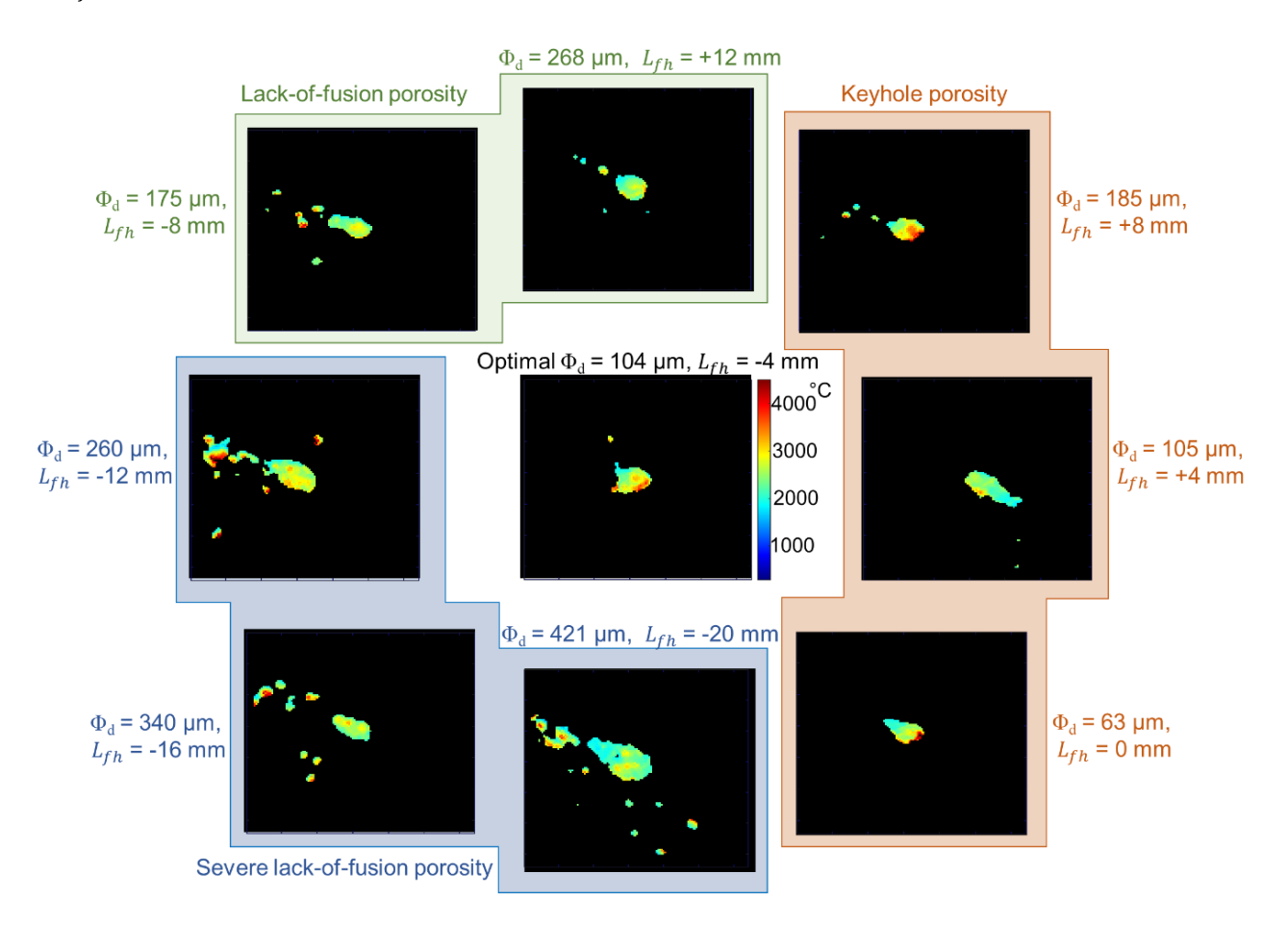


Figure 16: Representative temperature field images of cylinders built under different laser spot sizes (Φ_d) and laser focus height (L_{fh}) . Sample temperature field videos from the four above-shown regimes, viz. severe lack-of-fusion porosity, keyhole porosity, optimal porosity, and lack-of-fusion porosity, are given Appendix B.

A quantitative comparison of the mean melt pool temperature as a function of laser spot size is presented in Figure 17. The lowest mean melt pool temperatures of ~2300 °C to 2500 °C are

observed when the laser is focused above the powder bed (L_{fh} = -12 mm to L_{fh} = -20 mm) corresponding to a laser spot size of Φ_d = 421 μ m to Φ_d = 175 μ m. Accordingly, the lack-of-fusion porosity is most severe under these conditions as there is insufficient energy melt material significantly below the surface. This is despite the melt pool temperature significantly exceeding the melting point of stainless steel 316L (~1400 °C) [29].

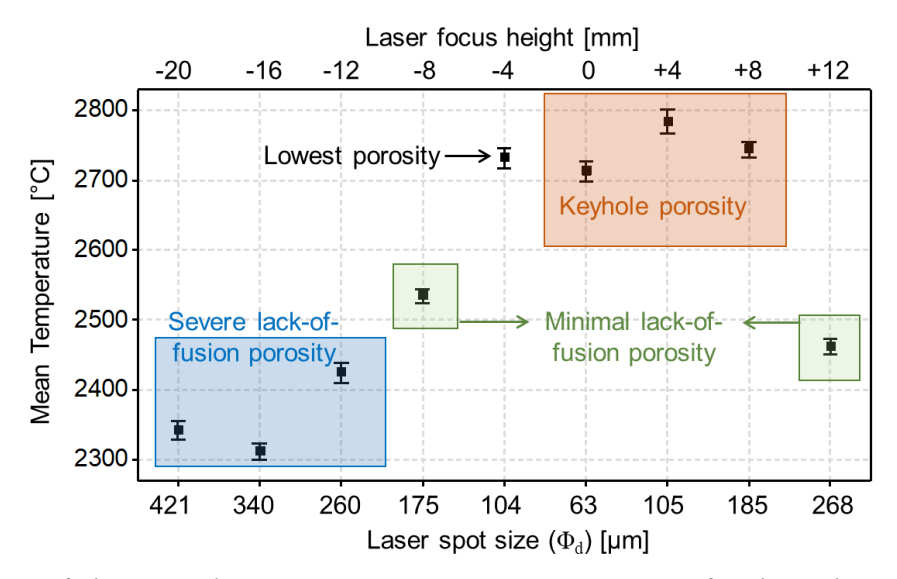


Figure 17: Effect of change in laser spot size on mean temperature of melt pool extracted from the temperature field images. Error bar is 1 standard deviation, and 1000 samples were used.

The mean melt pool temperature increases almost linearly as the focal plane approaches the powder bed ($\Phi_d = 104 \mu m$, $L_{fh} = -4 \text{ mm}$) and correlates to a reduction in lack-of-fusion porosity (Video B.2, Appendix B). The highest mean melt pool temperature of ~2800 °C (almost twice the melting temperature of SS 316L) is observed when the laser is focused at the build plane ($\Phi_d = 63 \mu m$, $L_{fh} = 0 \text{ mm}$) and is linked to keyhole porosity. A significant drop in melt pool temperature is observed as the focal plane of the laser deviates considerably below the powder bed to $L_{fh} = +12 \text{ mm}$.

A key point in Figure 17 is that the melt pool temperature of ~2750 °C results in minimal porosity as well as keyhole porosity. Figure 17 thus exemplifies that using the melt pool temperature

alone to predict the state of the process would not be sufficient; the shape (morphology) of the melt pool and the spatter behavior must also be accounted. In other words, there is a need to combine process signatures that capture the melt pool morphology, spatter characteristics, and melt pool temperature to improve process monitoring. The need is underscored in the forthcoming Sec. 3.4.

3.4 Prediction of laser spot size deviation (Task 1) and type of porosity (Task 2)

First, the melt pool morphology and temperature extracted from the high-speed camera and temperature field images were used separately, as well as together as inputs to various machine learning models to predict the laser spot size and the type of porosity. Figure 18 (a) and (b) show the correlation between three of the features extracted from the high-speed camera and temperature field images in terms of three different laser spot sizes (421 μm, 104 μm, and 268 μm), respectively. Although, the features amiably cluster the different laser spot sizes, considerable overlap between the clusters is evident due to the inherent non-linearity (Figure 15 and Figure 17). It is difficult, if not impossible, to demarcate these clusters with simple statistical regression analysis.

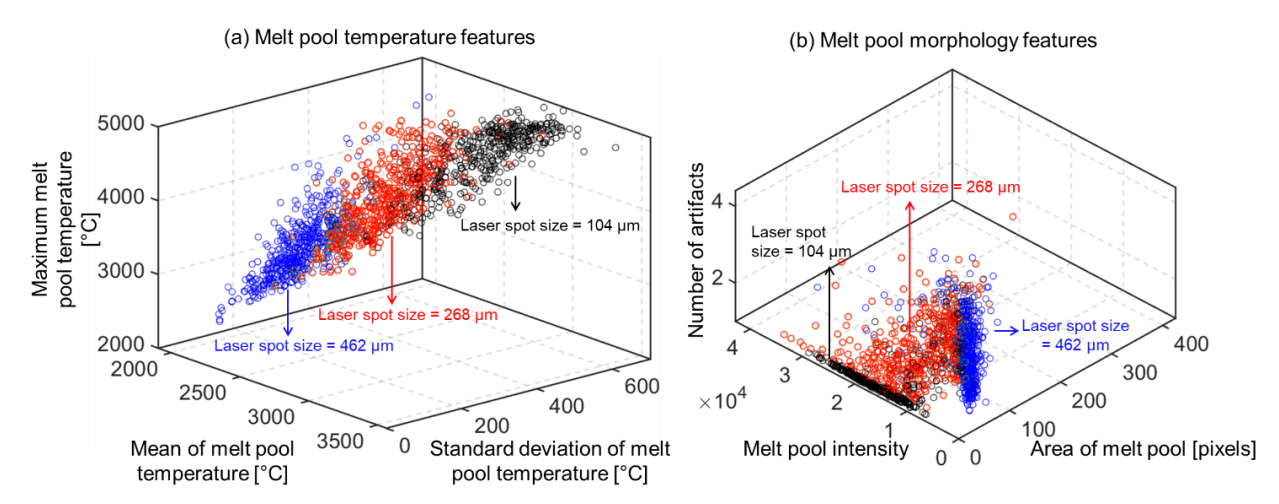


Figure 18: Correlations between features extracted from (a) temperature field images and (b) high-speed video camera images in terms of three laser focus heights-20 mm, -4 mm, and +12 mm. The three laser focus heights can be demarcated based on these features, but some overlap and nonlinearity are evident necessitating the use of machine learning models.

Hence, machine learning models are needed as they are capable of demarcating these regimes as they can create nonlinear decision boundaries [84]. To further illustrate this point, Table 4 reports the classification accuracy of the conventional statistical models – ridge regression-based classifier (RRC) and nonlinear logistic regression classifier (NLR) for distinguishing the type of porosity and laser spot size in terms of the F1-score. The false positive rate (FPR) and false negative rate (FNR) are reported in Table 5. From Table 4 it is apparent that the conventional statistical models yield an F1-score in the range of 70% to 85%, noting that the prediction accuracy is considerably improved when both melt pool morphology and spatter characteristics, and temperature features are combined.

To further improve this prediction accuracy, the following machine learning models were tested: multilayer perceptron (MLP), random forest (RF), support vector machine (SVM), k-nearest neighbors (KNN), and deep learning convolutional neural network (CNN). We reiterate that the CNN does not use the physics-based melt pool features (Sec. 2.4) but employs the raw melt pool images directly. Indeed, the relatively simple SVM machine learning model resulted in a F1-score of 0.95 in 9-way classification when the melt pool morphology and spatter, and temperature are used together. In contrast, the same SVM model provides a F-score of 0.84 and 0.65, respectively, when either the melt pool morphology and spatter, or temperature filed are used in isolation. This prediction fidelity was found to be at par to the complex convolutional neural network (CNN) that uses the raw melt pool images instead of the physics-based data signatures [55]. Considering computational and interpretability advantages, using low-level, intuitive, and process physics-based features with relatively simple machine learning models is a viable alternative to CNN.

Figure 19 (a) and (b) reinforce the two key results reported in Table 4 for laser spot size and type of porosity classification, respectively. First, using physically intuitive features with simple machine learning models, such as SVM, performs at par to complex deep learning CNN (Hypothesis

1) resulting in F1-score of ~95%. Second, combining the melt pool morphology and spatter signatures (A) and melt pool temperature features (B) considerably improves the classification accuracy of both the machine learning tasks.

Table 4: Laser spot size and type of porosity classification results using various machine learning and conventional statistical models. The classification fidelity is reported for the test dataset in terms of the F1-score.

Task 1 – determine laser spot size deviation											
Sensor features	RRC	NLR	KNN	RF	MLP	SVM	CNN				
(A) Melt pool morphology and spatter signatures	0.51	0.57	0.81	0.82	0.80	0.84	0.97				
(B) Melt pool temperature distribution	0.43	0.57	0.58	0.64	0.67	0.67	0.96				
A+B (data fusion)	0.67	0.82	0.87	0.89	0.95	0.95	0.96				
Task 2 – determine type of porosity											
Sensor features	RRC	NLR	KNN	RF	MLP	SVM	CNN				
(A) Melt pool morphology and spatter signatures	0.71	0.76	0.96	0.97	0.96	0.87	0.95				
(B) Melt pool temperature distribution	0.60	0.62	0.85	0.87	0.89	0.75	0.92				
A+B (data fusion)	0.77	0.84	0.97	0.98	0.98	0.94	0.94				

Table 5: Laser spot size and type of porosity classification results using ridge regression-based classifier (RRC), nonlinear logistic regression (NLR) k-nearest neighbors (KNN), multilayer perceptron (MLP), random forest (RF), support vector machine (SVM), and convolutional neural network (CNN). The classification fidelity is reported for the test dataset in terms of the false positive rate (FPR) and false negative rate (FNR). A = melt pool morphology and spatter signatures, B = melt pool temperature distribution, A+B = data fusion.

Task 1 – determine laser spot size deviation														
Sensor	RI	RC	NI	LR	KNN		MLP		RF		SVM		CNN	
features	FPR	FNR	FPR	FNR	FPR	FNR	FPR	FNR	FPR	FNR	FPR	FNR	FPR	FNR
A	0.02	0.19	0.07	0.39	0.02	0.19	0.02	0.20	0.02	0.17	0.02	0.16	0.002	0.03
В	0.05	0.41	0.05	0.41	0.05	0.41	0.04	0.32	0.04	0.36	0.04	0.32	0.001	0.05
A+B	0.01	0.12	0.02	0.17	0.01	0.12	0.006	0.05	0.01	0.10	0.005	0.04	0.002	0.05
Task 2 – determine type of porosity														
Sensor	RI	RC	C NLR		KNN MI		LP	P RF		SVM		CNN		
features	FPR	FNR	FPR	FNR	FPR	FNR	FPR	FNR	FPR	FNR	FPR	FNR	FPR	FNR
A	0.09	0.28	0.07	0.22	0.02	0.06	0.03	0.06	0.02	0.03	0.04	0.12	0.006	0.06
В	0.13	0.39	0.13	0.37	0.06	0.15	0.04	0.13	0.05	0.11	0.08	0.24	0.02	0.07
A+B	0.07	0.22	0.05	0.15	0.01	0.06	0.01	0.04	0.01	0.04	0.01	0.05	0.01	0.05

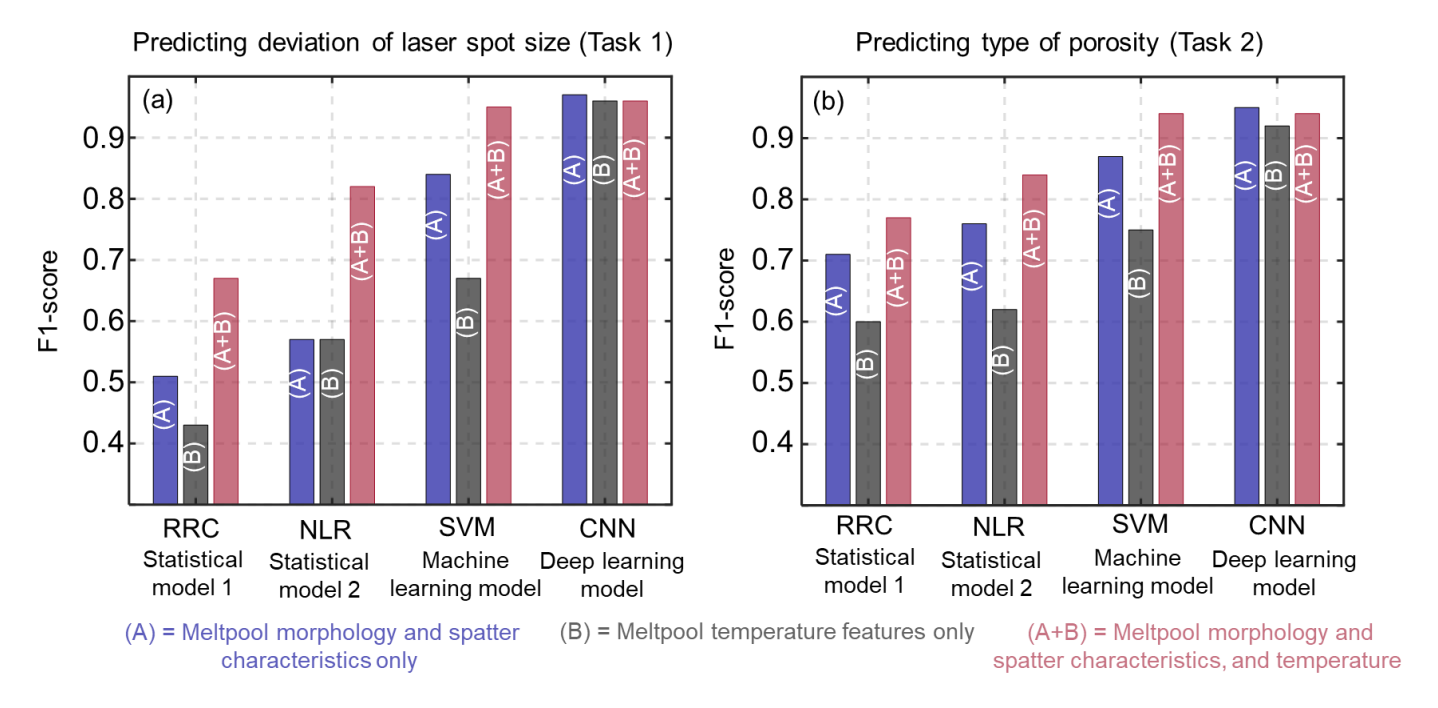


Figure 19: Graphical representation of the performance of different models used to classify the (a) laser spot size and (b) type of porosity in terms of F1-score. RRC = ridge regression classifier, NLR = nonlinear logistics regression classifier, SVM = support vector machine classifier, CNN = convolutional neural network classifier.

Table 5 reports the laser focus height prediction accuracy in terms of false positive rate (FPR) and false negative rate (FNR) of various machine learning models. Again, a notable improvement in the laser focus height prediction accuracy (reduced FPR and FNR) is observed when the features extracted from the high-speed video camera and temperature field images are used together. With the exemplar SVM model, the FPR with the melt pool morphology (A) and temperature signatures (B) was 0.02 and 0.04 respectively. This FPR reduced to 0.005 when both types of features were combined. A similarly significant reduction in FNR is observed using data fusion.

Further, plotted in Figure 20 are the receiver operating characteristics (ROC) curves and area under the curve (AUC) of the SVM model while performing laser spot size prediction using melt pool morphology and spatter characteristics, and temperature features by themselves and together. The plot in Figure 20 (d), suggest that the sensor data fusion yields AUC values very close to 1.00 when the SVM is applied to demarcate between laser spot size. Figure 20 (c) shows that the sensor

data fusion yields significantly improved performance compared to treating the data separately (Figure 20 (a) and (b)). The fused data shows very low false positive rates (~10⁻³) whilst maintaining an acceptable true positive rate (~0.9). At the same true positive rate, the melt pool morphology or temperature feature methods have a false positive rate of ~0.1 when analyzed separately. In other words, for an in-focus system the data fusion method would be capable of only raising a false alarm every 1 in 1000 predictions, whilst still flagging 9 out of 10 focus problems correctly. Depending on the application, this level of performance gives a machine operator significant confidence in the detection system, enabling routine industrial deployment of in-situ monitoring systems.

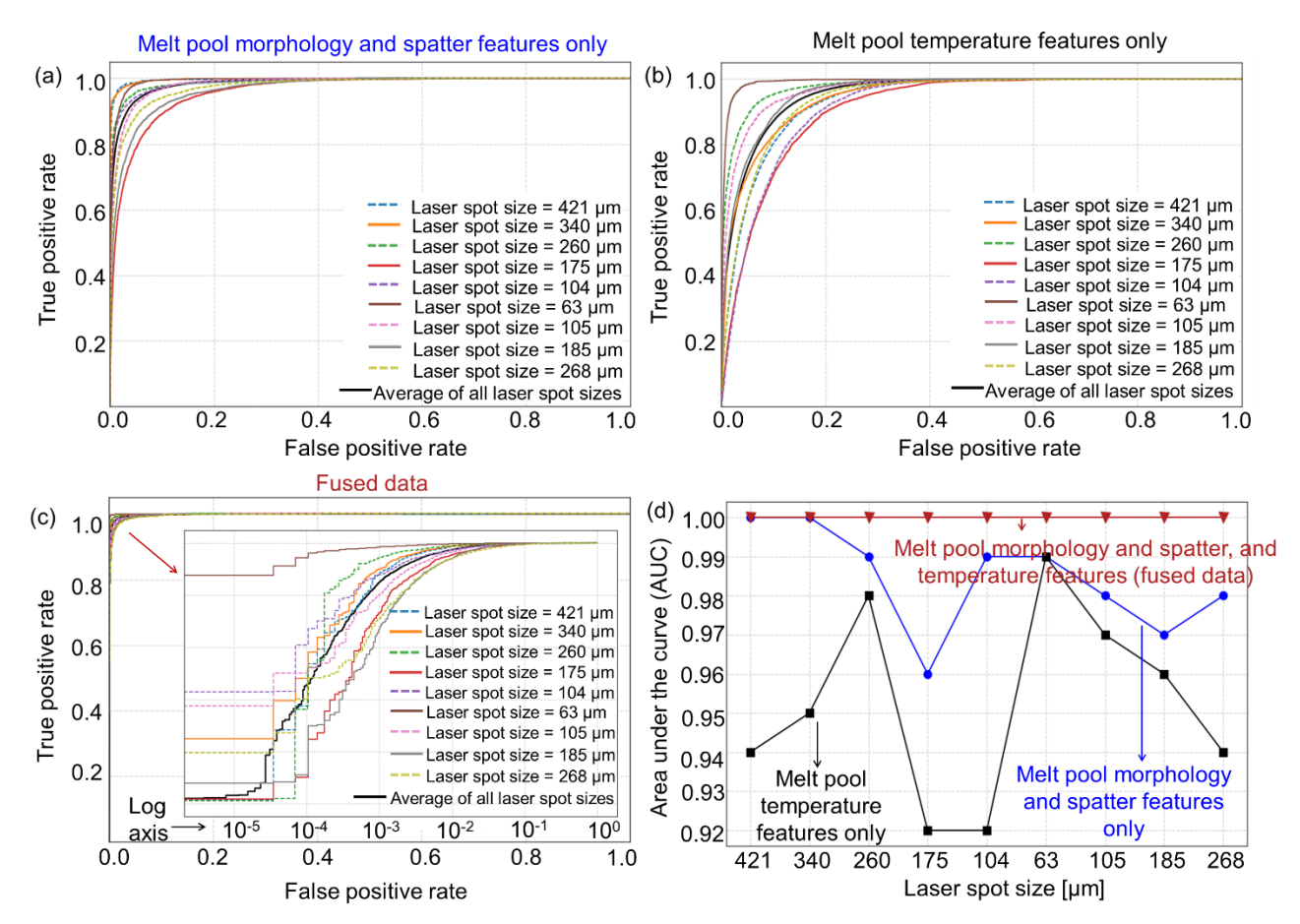


Figure 20: Receiver operating characteristic (ROC) curve and area under the curve (AUC) of 9-way laser spot size classification using Support Vector Machine (SVM). ROC curves when (a) only melt pool morphology features were used (F1-score = 0.84), (b) only melt pool temperature features were used (F1-score = 0.67), and (c) both melt pool morphology and temperature features were used (F1-score = 0.95). (d) AUC values of SVM when different feature sets were used for laser spot size classification.

4 Conclusions

In this work, we developed and applied an approach for in-process monitoring of the laser powder bed fusion (LPBF) additive manufacturing process using data acquired from a high-speed video camera and a melt pool temperature imaging system. The novelty of the approach is that it combines multiple physics-informed process signatures concerning the melt pool morphology, spatter characteristics, and melt pool temperature distribution with computationally light machine learning models.

The results affirm two hypotheses: (i) using data representative of multiple process phenomena, as opposed to one type of signature, significantly improves prediction of process anomalies and flaw formation; and (ii) the use of pragmatic physics-informed process signatures in simple machine learning models, such as support vector machine (SVM) and multilayer perceptron (MLP), is as effective as a complex, black-box deep learning convolutional neural network (CNN) for flaw detection.

Combining the melt pool morphology and spatter characteristics with melt pool temperature distribution features significantly improved the detection performance. Out of the various data-driven models tested, the statistical models had the least prediction fidelity (F1-score < 70%), while the CNN, MLP and SVM showed comparable results with F1-score of \sim 95%. The receiver operating characteristic curve analysis highlighted the advantage of data fusion; the false positive rates reduced from \sim 0.1 when treating data signatures independently to \sim 10⁻³ when signatures were fused without sacrificing the true positive rate (\sim 0.9). This marks a significant step forward towards deployment of industrially relevant and practically viable LPBF in-process monitoring systems.

Acknowledgements

Paul A. Hooper, Harry de Winton, and Richard J. Williams thank AWE plc (contract 30338995) and EPSRC (EP/K503733/1, EP/R513052/1) for their financial support for this research.

Prahalada Rao thanks the National Science Foundation (NSF) and Department of Energy (DoE) for funding his work under awards OIA-1929172, CMMI-1920245, CMMI-1739696, ECCS-2020246, PFI-TT 2044710, CMMI-1752069, CMMI-1719388, and DE-SC0021136. Understanding the causal influence of process parameters on part quality and detection of defect formation using insitu sensing was the major aspect of CMMI-1752069 (Program Officer: Kevin Chou). The use of AI algorithms for defect detection in additive manufacturing was proposed in ECCS-2020246 (Program Officer: Donald Wunsch). Supplemental funding for CMMI-1752069 was obtained through the NSF INTERN program (Program Officer: Prakash Balan) and CMMI Data Science Activities (Program Officer: Martha Dodson) is greatly appreciated. The later supplement funded Ziyad Smoqi and Aniruddha Gaikwad's research. The X-ray CT analysis was conducted on the instrument partially funded through the Major Research instrumentation grant (CMMI-1920245, program officer: Wendy C. Crone). Ben Bevans' work was funded partially through the DoE Grant DE-SC0021136. The materials characterization research was performed in part in the Nebraska Nanoscale Facility: National Nanotechnology Coordinated Infrastructure under award no. ECCS: 2025298, and with support from the Nebraska Research Initiative through the Nebraska Center for Materials and Nanoscience and the Nanoengineering Research Core Facility at the University of Nebraska-Lincoln.

Data Availability

The raw/processed data required to reproduce these findings cannot be shared at this time as the data also forms part of an ongoing study.

Appendices

Appendix A: Representative high-speed videos

Video A.1: High-speed video acquired under the laser spot size that yielded severe lack-of-fusion porosity. File name: HSV severe lack of fusion porosity.avi

Video A.2: High-speed video acquired under the laser spot size that yielded the lowest porosity. File name: HSV_lowest_porosity.avi

Video A.3: High-speed video acquired under the laser spot size that yielded keyhole porosity. File name: HSV_keyhole_porosity.avi

Video A.4: High-speed video acquired under the laser spot size that yielded the lack of fusion porosity. File name: HSV lack of fusion porosity.avi

Note: The pixel values in the above-mentioned videos are intensity readings.

Appendix B: Representative temperature field videos

Video B.1: Temperature field video acquired under the laser spot size that yielded severe lack-of-fusion porosity. File name: Temperature _severe_lack_of_fusion_porosity.avi

Video B.2: Temperature field video acquired under the laser spot size that yielded the lowest porosity. File name: Temperature _lowest_porosity.avi

Video B.3: Temperature field video acquired under the laser spot size that yielded keyhole porosity. File name: Temperature _keyhole_porosity.avi

Video B.4: Temperature field video acquired under the laser spot size that yielded the lack of fusion porosity. File name: Temperature lack of fusion porosity.avi

Note: The pixel values in the above-mentioned videos are temperature readings in degree Celsius (°C).

Appendix C: High-speed spatter video

Video C.1: High-speed video acquired from near-coaxial camera that elucidates the spatter characteristics that were observed when the laser was out of focus. File name: Laser_out_of_focus.avi

References

- [1] Sames, W. J., List, F. A., Pannala, S., Dehoff, R. R., and Babu, S. S., 2016, "The metallurgy and processing science of metal additive manufacturing," International Materials Reviews, 61(5), pp. 315-360.doi:10.1080/09506608.2015.1116649
- [2] Guo, N., and Leu, M. C., 2013, "Additive manufacturing: technology, applications and research needs," Frontiers of Mechanical Engineering, 8(3), pp. 215-243.doi:10.1007/s11465-013-0248-8
- [3] Grasso, M., and Colosimo, B. M., 2017, "Process defects and in situmonitoring methods in metal powder bed fusion: a review," Measurement Science and Technology, 28(4), p. 044005.doi:10.1088/1361-6501/aa5c4f
- [4] Mani, M., Lane, B. M., Donmez, M. A., Feng, S. C., and Moylan, S. P., 2017, "A review on measurement science needs for real-time control of additive manufacturing metal powder bed fusion processes," International Journal of Production Research, 55(5), pp. 1400-1418.doi:10.1080/00207543.2016.1223378
- [5] Tapia, G., and Elwany, A., 2014, "A Review on Process Monitoring and Control in Metal-Based Additive Manufacturing," Journal of Manufacturing Science and Engineering, 136(6).doi:10.1115/1.4028540
- [6] Spears, T. G., and Gold, S. A., 2016, "In-process sensing in selective laser melting (SLM) additive manufacturing," Integrating Materials and Manufacturing Innovation, 5(1), pp. 16-40.doi:10.1186/s40192-016-0045-4
- [7] Everton, S. K., Hirsch, M., Stravroulakis, P., Leach, R. K., and Clare, A. T., 2016, "Review of in-situ process monitoring and in-situ metrology for metal additive manufacturing," Materials & Design, 95, pp. 431-445.doi:https://doi.org/10.1016/j.matdes.2016.01.099
- [8] Grasso, M., Remani, A., Dickins, A., Colosimo, B. M., and Leach, R. K., 2021, "In-situ measurement and monitoring methods for metal powder bed fusion: an updated review," Measurement Science and Technology, 32(11), p. 112001.doi:10.1088/1361-6501/ac0b6b
- [9] King, W. E., Anderson, A. T., Ferencz, R. M., Hodge, N. E., Kamath, C., Khairallah, S. A., and Rubenchik, A. M., 2015, "Laser powder bed fusion additive manufacturing of metals; physics, computational, and materials challenges," Applied Physics Reviews, 2(4), p. 041304.doi:10.1063/1.4937809
- [10] Polonsky, A. T., and Pollock, T. M., 2020, "Closing the science gap in 3D metal printing," Science, 368(6491), pp. 583-584.doi:doi:10.1126/science.abb4938
- [11] Snow, Z., Nassar, A. R., and Reutzel, E. W., 2020, "Invited Review Article: Review of the formation and impact of flaws in powder bed fusion additive manufacturing," Additive Manufacturing, 36, p. 101457.doi:https://doi.org/10.1016/j.addma.2020.101457
- [12] Faidel, D., Laskin, A., Behr, W., and Natour, G., 2016, "Improvement of selective laser melting by beam shaping and minimized thermally induced effects in optical systems," International Conference on Photonic Technologies LANE,
- [13] Deisenroth, D. C., Neira, J., Weaver, J., and Yeung, H., 2020, "Effects of Shield Gas Flow on Meltpool Variability and Signature in Scanned Laser Melting," ASME 2020 15th International Manufacturing Science and Engineering Conference.

- [14] Goossens, L. R., Kinds, Y., Kruth, J.-P., and Van Hooreweder, B., 2018, "On the influence of thermal lensing during selective laser melting," Solid freeform fabrication symposium proceedings (SFF Symp 2018), pp. 2267-2274
- [15] Yavari, R., Riensche, A., Tekerek, E., Jacquemetton, L., Halliday, H., Vandever, M., Tenequer, A., Perumal, V., Kontsos, A., Smoqi, Z., Cole, K., and Rao, P., 2021, "Digitally twinned additive manufacturing: Detecting flaws in laser powder bed fusion by combining thermal simulations with in-situ meltpool sensor data," Materials & Design, 211, p. 110167.doi:https://doi.org/10.1016/j.matdes.2021.110167
- [16] Williams, R. J., Piglione, A., Rønneberg, T., Jones, C., Pham, M.-S., Davies, C. M., and Hooper, P. A., 2019, "In situ thermography for laser powder bed fusion: Effects of layer temperature on porosity, microstructure and mechanical properties," Additive Manufacturing, 30, p. 100880.doi:https://doi.org/10.1016/j.addma.2019.100880
- [17] Hojjatzadeh, S. M. H., Parab, N. D., Guo, Q., Qu, M., Xiong, L., Zhao, C., Escano, L. I., Fezzaa, K., Everhart, W., Sun, T., and Chen, L., 2020, "Direct observation of pore formation mechanisms during LPBF additive manufacturing process and high energy density laser welding," International Journal of Machine Tools and Manufacture, 153, p. 103555.doi:https://doi.org/10.1016/j.ijmachtools.2020.103555
- [18] Yavari, R., Smoqi, Z., Riensche, A., Bevans, B., Kobir, H., Mendoza, H., Song, H., Cole, K., and Rao, P., 2021, "Part-scale thermal simulation of laser powder bed fusion using graph theory: Effect of thermal history on porosity, microstructure evolution, and recoater crash," Materials & Design, 204, p. 109685.doi:https://doi.org/10.1016/j.matdes.2021.109685
- [19] Khairallah, S. A., Anderson, A. T., Rubenchik, A., and King, W. E., 2016, "Laser powder-bed fusion additive manufacturing: Physics of complex melt flow and formation mechanisms of pores, spatter, and denudation zones," Acta Materialia, 108, pp. 36-45.doi:https://doi.org/10.1016/j.actamat.2016.02.014
- [20] Seifi, M., Gorelik, M., Waller, J., Hrabe, N., Shamsaei, N., Daniewicz, S., and Lewandowski, J. J., 2017, "Progress Towards Metal Additive Manufacturing Standardization to Support Qualification and Certification," JOM, 69(3), pp. 439-455.doi:10.1007/s11837-017-2265-2
- [21] Seifi, M., Salem, A., Beuth, J., Harrysson, O., and Lewandowski, J. J., 2016, "Overview of Materials Qualification Needs for Metal Additive Manufacturing," JOM, 68(3), pp. 747-764.doi:10.1007/s11837-015-1810-0
- [22] Qin, J., Hu, F., Liu, Y., Witherell, P., Wang, C. C. L., Rosen, D. W., Simpson, T. W., Lu, Y., and Tang, Q., 2022, "Research and application of machine learning for additive manufacturing," Additive Manufacturing, 52, p. 102691.doi:https://doi.org/10.1016/j.addma.2022.102691
- [23] Smoqi, Z., Gaikwad, A., Bevans, B., Kobir, M. H., Craig, J., Abul-Haj, A., Peralta, A., and Rao, P., 2022, "Monitoring and Prediction of Porosity in Laser Powder Bed Fusion using Physics-informed Meltpool Signatures and Machine Learning," Journal of Materials Processing Technology, p. 117550.doi:https://doi.org/10.1016/j.jmatprotec.2022.117550
- [24] Montazeri, M., Yavari, R., Rao, P., and Boulware, P., 2018, "In-Process Monitoring of Material Cross-Contamination Defects in Laser Powder Bed Fusion," Journal of Manufacturing Science and Engineering, 140(11).doi:10.1115/1.4040543

- [25] Huang, Y., Leu, M. C., Mazumder, J., and Donmez, A., 2015, "Additive Manufacturing: Current State, Future Potential, Gaps and Needs, and Recommendations," Journal of Manufacturing Science and Engineering, 137(1).doi:10.1115/1.4028725
- [26] Wang, C., Tan, X. P., Tor, S. B., and Lim, C. S., 2020, "Machine learning in additive manufacturing: State-of-the-art and perspectives," Additive Manufacturing, 36, p. 101538.doi:https://doi.org/10.1016/j.addma.2020.101538
- [27] Meng, L., McWilliams, B., Jarosinski, W., Park, H.-Y., Jung, Y.-G., Lee, J., and Zhang, J., 2020, "Machine Learning in Additive Manufacturing: A Review," JOM, 72(6), pp. 2363-2377.doi:10.1007/s11837-020-04155-y
- [28] de Winton, H. C., Cegla, F., and Hooper, P. A., 2021, "A method for objectively evaluating the defect detection performance of in-situ monitoring systems," Additive Manufacturing, 48, p. 102431.doi:https://doi.org/10.1016/j.addma.2021.102431
- [29] Hooper, P. A., 2018, "Melt pool temperature and cooling rates in laser powder bed fusion," Additive Manufacturing, 22, pp. 548-559.doi:https://doi.org/10.1016/j.addma.2018.05.032
- [30] DebRoy, T., Wei, H. L., Zuback, J. S., Mukherjee, T., Elmer, J. W., Milewski, J. O., Beese, A. M., Wilson-Heid, A., De, A., and Zhang, W., 2018, "Additive manufacturing of metallic components Process, structure and properties," Progress in Materials Science, 92, pp. 112-224.doi:https://doi.org/10.1016/j.pmatsci.2017.10.001
- [31] Khairallah Saad, A., Martin Aiden, A., Lee Jonathan, R. I., Guss, G., Calta Nicholas, P., Hammons Joshua, A., Nielsen Michael, H., Chaput, K., Schwalbach, E., Shah Megna, N., Chapman Michael, G., Willey Trevor, M., Rubenchik Alexander, M., Anderson Andrew, T., Wang, Y. M., Matthews Manyalibo, J., and King Wayne, E., 2020, "Controlling interdependent meso-nanosecond dynamics and defect generation in metal 3D printing," Science, 368(6491), pp. 660-665.doi:10.1126/science.aay7830
- [32] Matthews, M. J., Guss, G., Khairallah, S. A., Rubenchik, A. M., Depond, P. J., and King, W. E., 2016, "Denudation of metal powder layers in laser powder bed fusion processes," Acta Materialia, 114, pp. 33-42.doi:https://doi.org/10.1016/j.actamat.2016.05.017
- [33] King, W. E., Barth, H. D., Castillo, V. M., Gallegos, G. F., Gibbs, J. W., Hahn, D. E., Kamath, C., and Rubenchik, A. M., 2014, "Observation of keyhole-mode laser melting in laser powder-bed fusion additive manufacturing," Journal of Materials Processing Technology, 214(12), pp. 2915-2925.doi:https://doi.org/10.1016/j.jmatprotec.2014.06.005
- [34] Repossini, G., Laguzza, V., Grasso, M., and Colosimo, B. M., 2017, "On the use of spatter signature for in-situ monitoring of Laser Powder Bed Fusion," Additive Manufacturing, 16, pp. 35-48.doi:https://doi.org/10.1016/j.addma.2017.05.004
- [35] Grasso, M., Laguzza, V., Semeraro, Q., and Colosimo, B. M., 2016, "In-Process Monitoring of Selective Laser Melting: Spatial Detection of Defects Via Image Data Analysis," Journal of Manufacturing Science and Engineering, 139(5).doi:10.1115/1.4034715
- [36] Groeber, M. A., Schwalbach, E., Donegan, S., Chaput, K., Butler, T., and Miller, J., 2017, "Application of characterization, modelling, and analytics towards understanding process-structure linkages in metallic 3D printing," IOP Conference Series: Materials Science and Engineering, 219, p. 012002.doi:10.1088/1757-899x/219/1/012002

- [37] Wang, D., Wu, S., Fu, F., Mai, S., Yang, Y., Liu, Y., and Song, C., 2017, "Mechanisms and characteristics of spatter generation in SLM processing and its effect on the properties," Materials & Design, 117, pp. 121-130.doi:https://doi.org/10.1016/j.matdes.2016.12.060
- [38] Simonelli, M., Tuck, C., Aboulkhair, N. T., Maskery, I., Ashcroft, I., Wildman, R. D., and Hague, R., 2015, "A Study on the Laser Spatter and the Oxidation Reactions During Selective Laser Melting of 316L Stainless Steel, Al-Si10-Mg, and Ti-6Al-4V," Metallurgical and Materials Transactions A, 46(9), pp. 3842-3851.doi:10.1007/s11661-015-2882-8
- [39] Guo, Q., Zhao, C., Qu, M., Xiong, L., Escano, L. I., Hojjatzadeh, S. M. H., Parab, N. D., Fezzaa, K., Everhart, W., Sun, T., and Chen, L., 2019, "In-situ characterization and quantification of melt pool variation under constant input energy density in laser powder bed fusion additive manufacturing process,"

 Additive Manufacturing, 28, pp. 600-609.doi:https://doi.org/10.1016/j.addma.2019.04.021
- [40] DePond, P. J., Fuller, J. C., Khairallah, S. A., Angus, J. R., Guss, G., Matthews, M. J., and Martin, A. A., 2020, "Laser-metal interaction dynamics during additive manufacturing resolved by detection of thermally-induced electron emission," Communications Materials, 1(1), p. 92.doi:10.1038/s43246-020-00094-y
- [41] Tang, M., Pistorius, P. C., and Beuth, J. L., 2017, "Prediction of lack-of-fusion porosity for powder bed fusion," Additive Manufacturing, 14, pp. 39-48.doi:https://doi.org/10.1016/j.addma.2016.12.001
- [42] Slotwinski, J. A., Garboczi, E. J., and Hebenstreit, K. M., 2014, "Porosity Measurements and Analysis for Metal Additive Manufacturing Process Control," J Res Natl Inst Stand Technol, 119, pp. 494-528.doi:10.6028/jres.119.019
- [43] Cunningham, R., Zhao, C., Parab, N., Kantzos, C., Pauza, J., Fezzaa, K., Sun, T., and Rollett, A. D., 2019, "Keyhole threshold and morphology in laser melting revealed by ultrahigh-speed x-ray imaging," Science, 363(6429), pp. 849-852
- [44] Snow, Z., Diehl, B., Reutzel, E. W., and Nassar, A., 2021, "Toward in-situ flaw detection in laser powder bed fusion additive manufacturing through layerwise imagery and machine learning," Journal of Manufacturing Systems, 59, pp. 12-26.doi:https://doi.org/10.1016/j.jmsy.2021.01.008
- [45] Mostafaei, A., Zhao, C., He, Y., Reza Ghiaasiaan, S., Shi, B., Shao, S., Shamsaei, N., Wu, Z., Kouraytem, N., Sun, T., Pauza, J., Gordon, J. V., Webler, B., Parab, N. D., Asherloo, M., Guo, Q., Chen, L., and Rollett, A. D., 2022, "Defects and anomalies in powder bed fusion metal additive manufacturing," Current Opinion in Solid State and Materials Science, 26(2), p. 100974.doi:https://doi.org/10.1016/j.cossms.2021.100974
- [46] Imani, F., Gaikwad, A., Montazeri, M., Rao, P., Yang, H., and Reutzel, E., 2018, "Process Mapping and In-Process Monitoring of Porosity in Laser Powder Bed Fusion Using Layerwise Optical Imaging," Journal of Manufacturing Science and Engineering, 140(10).doi:10.1115/1.4040615
- [47] Artzt, K., Siggel, M., Kleinert, J., Riccius, J., Requena, G., and Haubrich, J., 2020, "Pyrometric-Based Melt Pool Monitoring Study of CuCr1Zr Processed Using L-PBF," Materials, 13(20).doi:10.3390/ma13204626
- [48] Scipioni Bertoli, U., Wolfer, A. J., Matthews, M. J., Delplanque, J.-P. R., and Schoenung, J. M., 2017, "On the limitations of Volumetric Energy Density as a design parameter for Selective

- Laser Melting," Materials & Design, 113, pp. 331-340.doi:https://doi.org/10.1016/j.matdes.2016.10.037
- [49] Smoqi, Z., Bevans, B. D., Gaikwad, A., Craig, J., Abul-Haj, A., Roeder, B., Macy, B., Shield, J. E., and Rao, P., 2022, "Closed-loop control of meltpool temperature in directed energy deposition," Materials & Design, 215, p. 110508.doi:https://doi.org/10.1016/j.matdes.2022.110508
- [50] Dhanachandra, N., Manglem, K., and Chanu, Y. J., 2015, "Image Segmentation Using K-means Clustering Algorithm and Subtractive Clustering Algorithm," Procedia Computer Science, 54, pp. 764-771.doi:https://doi.org/10.1016/j.procs.2015.06.090
- [51] Nassar, A. R., Gundermann, M. A., Reutzel, E. W., Guerrier, P., Krane, M. H., and Weldon, M. J., 2019, "Formation processes for large ejecta and interactions with melt pool formation in powder bed fusion additive manufacturing," Scientific Reports, 9(1), p. 5038.doi:10.1038/s41598-019-41415-7
- [52] Ali, U., Esmaeilizadeh, R., Ahmed, F., Sarker, D., Muhammad, W., Keshavarzkermani, A., Mahmoodkhani, Y., Marzbanrad, E., and Toyserkani, E., 2019, "Identification and characterization of spatter particles and their effect on surface roughness, density and mechanical response of 17-4 PH stainless steel laser powder-bed fusion parts," Materials Science and Engineering: A, 756, pp. 98-107.doi:https://doi.org/10.1016/j.msea.2019.04.026
- [53] Esmaeilizadeh, R., Ali, U., Keshavarzkermani, A., Mahmoodkhani, Y., Marzbanrad, E., and Toyserkani, E., 2019, "On the effect of spatter particles distribution on the quality of Hastelloy X parts made by laser powder-bed fusion additive manufacturing," Journal of Manufacturing Processes, 37, pp. 11-20.doi:https://doi.org/10.1016/j.jmapro.2018.11.012
- [54] Qiu, C., Panwisawas, C., Ward, M., Basoalto, H. C., Brooks, J. W., and Attallah, M. M., 2015, "On the role of melt flow into the surface structure and porosity development during selective laser melting," Acta Materialia, 96, pp. 72-79.doi:https://doi.org/10.1016/j.actamat.2015.06.004
- [55] Gaikwad, A., Giera, B., Guss, G. M., Forien, J.-B., Matthews, M. J., and Rao, P., 2020, "Heterogeneous sensing and scientific machine learning for quality assurance in laser powder bed fusion A single-track study," Additive Manufacturing, 36, p. 101659.doi:https://doi.org/10.1016/j.addma.2020.101659
- [56] Li, E. L., Wang, L., Yu, A. B., and Zhou, Z. Y., 2021, "A three-phase model for simulation of heat transfer and melt pool behaviour in laser powder bed fusion process," Powder Technology, 381, pp. 298-312.doi:https://doi.org/10.1016/j.powtec.2020.11.061
- [57] Gardner, M. W., and Dorling, S. R., 1998, "Artificial neural networks (the multilayer perceptron)—a review of applications in the atmospheric sciences," Atmospheric Environment, 32(14), pp. 2627-2636.doi:https://doi.org/10.1016/S1352-2310(97)00447-0
- [58] Biau, G., and Scornet, E., 2016, "A random forest guided tour," TEST, 25(2), pp. 197-227.doi:10.1007/s11749-016-0481-7
- [59] Noble, W. S., 2006, "What is a support vector machine?," Nature Biotechnology, 24(12), pp. 1565-1567.doi:10.1038/nbt1206-1565
- [60] Mitchell, T. M., 1997, Machine Learning, McGraw-Hill.

- [61] Yuan, B., Guss, G. M., Wilson, A. C., Hau-Riege, S. P., DePond, P. J., McMains, S., Matthews, M. J., and Giera, B., 2018, "Machine-Learning-Based Monitoring of Laser Powder Bed Fusion," Advanced Materials Technologies, 3(12), p. 1800136.doi:https://doi.org/10.1002/admt.201800136
- [62] Williams, J., Dryburgh, P., Clare, A., Rao, P., and Samal, A., 2018, "Defect Detection and Monitoring in Metal Additive Manufactured Parts through Deep Learning of Spatially Resolved Acoustic Spectroscopy Signals," Smart and Sustainable Manufacturing Systems, 2(1), pp. 204-226.doi:10.1520/SSMS20180035
- [63] Yuan, B., Giera, B., Guss, G., Matthews, I., and Mcmains, S., 2019, "Semi-Supervised Convolutional Neural Networks for In-Situ Video Monitoring of Selective Laser Melting," 2019 IEEE Winter Conference on Applications of Computer Vision (WACV), pp. 744-753doi:10.1109/WACV.2019.00084.
- [64] Gonzalez-Val, C., Pallas, A., Panadeiro, V., and Rodriguez, A., 2020, "A convolutional approach to quality monitoring for laser manufacturing," Journal of Intelligent Manufacturing, 31(3), pp. 789-795.doi:10.1007/s10845-019-01495-8
- [65] Elwarfalli, H., Papazoglou, D., Erdahl, D., Doll, A., and Speltz, J., 2019, "In Situ Process Monitoring for Laser-Powder Bed Fusion using Convolutional Neural Networks and Infrared Tomography," 2019 IEEE National Aerospace and Electronics Conference (NAECON), pp. 323-327doi:10.1109/NAECON46414.2019.9058251.
- [66] Scime, L., and Beuth, J., 2018, "A multi-scale convolutional neural network for autonomous anomaly detection and classification in a laser powder bed fusion additive manufacturing process," Additive Manufacturing, 24, pp. 273-286.doi:https://doi.org/10.1016/j.addma.2018.09.034
- [67] Francis, J., and Bian, L., 2019, "Deep Learning for Distortion Prediction in Laser-Based Additive Manufacturing using Big Data," Manufacturing Letters, 20, pp. 10-14.doi:https://doi.org/10.1016/j.mfglet.2019.02.001
- [68] Ren, K., Chew, Y., Zhang, Y. F., Fuh, J. Y. H., and Bi, G. J., 2020, "Thermal field prediction for laser scanning paths in laser aided additive manufacturing by physics-based machine learning," Computer Methods in Applied Mechanics and Engineering, 362, p. 112734.doi:https://doi.org/10.1016/j.cma.2019.112734
- [69] Mozaffar, M., Liao, S., Lin, H., Ehmann, K., and Cao, J., 2021, "Geometry-Agnostic Data-Driven Thermal Modeling of Additive Manufacturing Processes using Graph Neural Networks," Additive Manufacturing, p. 102449.doi:https://doi.org/10.1016/j.addma.2021.102449
- [70] Becker, P., Roth, C., Roennau, A., and Dillmann, R., 2020, "Acoustic Anomaly Detection in Additive Manufacturing with Long Short-Term Memory Neural Networks," 2020 IEEE 7th International Conference on Industrial Engineering and Applications (ICIEA), pp. 921-926doi:10.1109/ICIEA49774.2020.9102002.
- [71] Ho, S., Zhang, W., Young, W., Buchholz, M., Jufout, S. A., Dajani, K., Bian, L., and Mozumdar, M., 2021, "DLAM: Deep Learning Based Real-Time Porosity Prediction for Additive Manufacturing Using Thermal Images of the Melt Pool," IEEE Access, 9, pp. 115100-115114.doi:10.1109/ACCESS.2021.3105362
- [72] Hertlein, N., Buskohl, P. R., Gillman, A., Vemaganti, K., and Anand, S., 2021, "Generative adversarial network for early-stage design flexibility in topology optimization for additive

- manufacturing," Journal of Manufacturing Systems, 59, pp. 675-685.doi:https://doi.org/10.1016/j.jmsy.2021.04.007
- [73] Gobert, C., Arrieta, E., Belmontes, A., Wicker, B., Medina, F., and McWilliams, B., 2019, "Conditional generative adversarial networks for in-situ layerwise additive manufacturing data," Proceeding of the 29th international Solid Freeform Fabrication Symposium, doi:10.20944/preprints202101.0519.v1.
- [74] Larsen, S., and Hooper, P. A., 2021, "Deep semi-supervised learning of dynamics for anomaly detection in laser powder bed fusion," Journal of Intelligent Manufacturing.doi: 10.1007/s10845-021-01842-8
- [75] Tan, Y., Jin, B., Nettekoven, A., Chen, Y., Yue, Y., Topcu, U., and Sangiovanni-Vincentelli, A., 2019, "An Encoder-Decoder Based Approach for Anomaly Detection with Application in Additive Manufacturing," 2019 18th IEEE International Conference On Machine Learning And Applications (ICMLA), pp. 1008-1015doi:10.1109/ICMLA.2019.00171.
- [76] Gaikwad, A., Imani, F., Yang, H., Reutzel, E., and Rao, P., 2019, "In Situ Monitoring of Thin-Wall Build Quality in Laser Powder Bed Fusion Using Deep Learning," Smart and Sustainable Manufacturing Systems, 3(1)
- [77] Montazeri, M., Nassar, A. R., Stutzman, C. B., and Rao, P., 2019, "Heterogeneous sensor-based condition monitoring in directed energy deposition," Additive Manufacturing, 30, p. 100916.doi:https://doi.org/10.1016/j.addma.2019.100916
- [78] Anguita, D., Ghio, A., Ridella, S., and Sterpi, D., 2009, "K-Fold Cross Validation for Error Rate Estimate in Support Vector Machines," DMIN, pp. 291-297
- [79] Xia, Y., Liu, C., Li, Y., and Liu, N., 2017, "A boosted decision tree approach using Bayesian hyper-parameter optimization for credit scoring," Expert Systems with Applications, 78, pp. 225-241.doi:https://doi.org/10.1016/j.eswa.2017.02.017
- [80] Gong, H., Rafi, K., Gu, H., Starr, T., and Stucker, B., 2014, "Analysis of defect generation in Ti–6Al–4V parts made using powder bed fusion additive manufacturing processes," Additive Manufacturing, 1-4, pp. 87-98.doi:https://doi.org/10.1016/j.addma.2014.08.002
- [81] Gaikwad, A., Yavari, R., Montazeri, M., Cole, K., Bian, L., and Rao, P., 2020, "Toward the digital twin of additive manufacturing: Integrating thermal simulations, sensing, and analytics to detect process faults," IISE Transactions, 52(11), pp. 1204-1217.doi:10.1080/24725854.2019.1701753
- [82] Montazeri, M., and Rao, P., 2018, "Sensor-Based Build Condition Monitoring in Laser Powder Bed Fusion Additive Manufacturing Process Using a Spectral Graph Theoretic Approach," Journal of Manufacturing Science and Engineering, 140(9).doi:10.1115/1.4040264
- [83] Montazeri, M., Nassar, A. R., Dunbar, A. J., and Rao, P., 2020, "In-process monitoring of porosity in additive manufacturing using optical emission spectroscopy," IISE Transactions, 52(5), pp. 500-515.doi:10.1080/24725854.2019.1659525
- [84] Wang, D., Zhang, M., Li, Z., Cui, Y., Liu, J., Yang, Y., and Wang, H., 2015, "Nonlinear decision boundary created by a machine learning-based classifier to mitigate nonlinear phase noise," 2015 European Conference on Optical Communication (ECOC), pp. 1-3doi:10.1109/ECOC.2015.7341753.